POLITECNICO DI MILANO

Scuola di Ingegneria Industriale e dell'Informazione

Corso di Laurea Magistrale in Ingegneria Nucleare

ANTI-COMPTON HAND-HELD PROBE FOR GAMMA SPECTROSCOPY IN HOMELAND SECURITY APPLICATIONS

Relatore: **Dott. Andrea POLA**

Correlatore: **Dott. Marco PETASECCA**

Tesi di Laurea Magistrale di:

Damiano CELESTE

Matricola: 784077

Anno Accademico 2012 - 2013

Ai miei genitori

"Iudico potere esser vero che la fortuna
sia arbitra della metá delle azioni nostre,
ma che etiam lei ne lasci governare
l'altra metá, o presso, a noi."
Niccoló Machiavelli

Acknowledgements

I would like to thank my committee member Doct. Andrea Pola who helped me to join the CMRP and supervised my work project and thesis from the beginning till the end.

I would like to express my deepest appreciation to Prof. Anatoly Rosenfeld, who gave me the opportunity to work with his research group at CMRP- University of Wollongong, and my supervisor Doct. Marco Petasecca who continually guided me during my internship and strongly conveyed an excitement in regard to physics research.

I would also like to thank the following people without whom this project would not have been possible:

Susanna Guatelli (Centre for Medical Radiation Physics, University of Wollongong).

Michael Weaver (Doctoral student at the Centre for Medical Radiation Physics, University of Wollongong).

Ringraziamenti

Cosa posso dirvi giunti al finale
se non ringraziarvi uno per uno,
a cominciare, se non vi par male,
da mamma e papá che a farmi studiare
han contribuito col capitale
e con la pazienza di chi sa amare,
cosí come vale e il mio nipitino,
il piú restio a farmi lavorare,
si son preoccupati del mio destino
permettendo l'avventura australiana.
Ringrazio zia Evi e mio cugino
perché ad ogni fine di settimana
chiedevan conto del mio percorso,
benché per la mia vita un po' mondana
non abbian mai fatto alcun esborso.
Non solo grazie alla mia famiglia
non son mai finito fuori corso,
ma anche per quella grande squadriglia
di amici lontani con cui in questo tempo
ho viaggiato per centomila miglia:
grazie ad Antonio, amico anzitempo,
passando dai Canna fino a Michele
storie da ricordare e, nel contempo,
io non dimentico Carlo e Daniele
i quali hanno fatto le loro parti.
Sempre pensando al tempo delle mele
ringrazio la Cami, pronta a aiutarti,
la Sili e ogni altro che con ardore
stava con te se volevi ubriacarti.
Cosí mi trovo a esser grato di cuore
anche a Mario, Matteo e poi Riccardo
che mi conobbero da seduttore...
...bene, lo ammetto, son stato bugiardo,
ma ció non mi vieta di ringraziare
chi con me a Parigi é stato goliardo.
Infine non posso non ricordare
chi gli ultimi anni m'ha vissuto appresso
e a questa Laurea mi ha fatto arrivare:
Gabri, con me dall'inizio ad adesso,
Sharma, col quale ho ancora un progetto
e con cui la Sessione fu un gran successo,
Diana con il suo fare spesso schietto,
e con i due Alberti, Anto e Chiara
si era tutti sotto lo stesso tetto.
Ora é finita codesta caciara,
non so in che luogo ci porterá il vento,
spesso vicende la vita separa
ma sará enorme il compiacimento
ogniqualvolta in cui il mio pensiero
volerá a voi, con ghigno contento.
Vi auguro il meglio e almeno spero
che questo Grazie vi sia parso bello...
...Mi scuserete son stato leggero
ma una persona manca all'appello.
Secondo il mio calcolo accurato
Sha se la ride come un pazzerello,
mentre costei ha l'occhio arrabbiato:
"niente citazioni" avevo promesso
ma finire senza aver ringraziato
Gaia con cui in effetti sto spesso
sarebbe sembrato alquanto sgarbato.

Abstract

Nowadays, controls on trafficking of illicit radioactive materials are increasingly important and more accurate techniques are required to detect and identify occulted radioisotopes such as highly depleted uranium and plutonium.

Gamma spectroscopy is one of the most powerful and non-invasive nuclear detection methods whose only limit is the detection of peaks at lower energies.

In order to solve this issue, the CMRP started developing an anti-Compton gamma-rays detector which is also a low-power and portable device. Based on a dual detector with two concentric CsI(Tl) scintillators, which are designed to be small in size and weight, and a Silicon Photomultiplier for light collection (PDE=13%), this detector has been conceived to be used in the field and in all conditions.

For this innovative dual detector design, the CMRP obtained a patent in the US and Chinese trades.

This project aimed to design and realise the first version of the electronics of this device. We realised an electronic circuit able to read out the SiPM outputs coming from the inner crystal and to shape them in order to obtain proper signals for spectroscopy. In parallel with this pulse-amplitude analysis, the timing analysis to veto Compton events was made possible by digitising signals coming from the outer crystal and turning them into 0-5V TTL signals which are able to control the logic gate in the MCA. In order to ensure the coincidence between signals associated to Compton events, a delay line was added to the inner channel.

Using a ^{137}Cs source and a dynamic range of 5V, we obtained shaped pulses with an amplitude of approximately 2V and a time width of 4μs in the inner channel. Concerning the outer channel, we chose a shaping time of 2μs obtaining pulses with a faster rising edge and amplitudes of the same order of magnitude. The delay time needed for the coincidence has been set at $400ns$.

Measurements of the Compton suppression efficiency have been done in the last part of this project. Changing the threshold voltage, the position of the source and the outer crystal shape and size, we optimised our system achieving an anti-Compton efficiency of 40.8%.

Light collection and consequently Compton suppression depend also on the volume and the surface quality of the outer scintillator: the best results were obtained using the newest conical shaped crystal. All measurements were done using a cylindrical 6x6mm inner scintillator, reaching an energy resolution of 9.3%.

Sommario

Attualmente i controlli di sicurezza sul traffico illecito di sostanze radioattive rivestono sempre maggiore importanza e tecniche via via più sofisticate devono essere sviluppate per rivelare e identificare radioisotopi occultati, come ad esempio Uranio altamente impoverito e Plutonio.

Uno dei metodi di rivelazione nucleare più performanti e meno invasivi utilizzati ad oggi è la spettroscopia gamma il cui principale limite è dato dalla scarsa efficienza a basse energie. Questo limite è dovuto al fatto che picchi di bassa intensità a basse energie sono spesso mascherati dal continuo Compton generato da emissioni gamma a più alta energia, cosicchè radioisotopi pericolosi o illegali possono essere nascosti se mescolati insieme ad altri radionuclidi (i.e. quelli per uso medico).

Al fine di porre rimedio a questo problema, il CMRP (Centre for Medical Radiation Physics) ha iniziato un percorso di sviluppo di un rivelatore gamma con soppressione Compton che si caratterizzi per i bassi consumi così come per la sua portatilità: basato su due cristalli scintillatori concentrici di CsI(Tl), progettati per avere dimensioni e peso ridotti al minimo, e sull'uso di un Silicon Photomultiplier (SiPM) come fotorivelatore, questo strumento è stato ideato per essere utilizzato sul campo e in ogni condizione climatica.

La configurazione duale e concentrica è necessaria per effettuare lo studio di spettroscopia attraverso il cristallo interno e per permettere, grazie al cristallo esterno, la rivelazione dei fotoni scatterati e quindi la soppressione Compton. Il SiPM, sostituendo i fototubi solitamente utilizzati in laboratorio per questo tipo di analisi, permette di realizzare un sistema che sia di dimensioni più ridotte e sia alimentato da tensioni molto minori.

Il CMRP ha già potuto brevettare questo design innovativo negli Stati Uniti e in Cina.

Il progetto in questione si è posto come obiettivo quello di progettare e realizzare la prima versione della componentistica elettronica dello strumento. Durante lo stage della durata di 7 mesi circa, abbiamo potuto realizzare l'elettronica in grado di leggere gli output del SiPM provenienti dal cristallo interno e modificare i segnali al fine di adeguarli ai parametri del MCA per la spettroscopia. In parallelo a questo canale interno, i segnali provenienti dal cristallo esterno vengono modellati e digitalizzati dalla stessa scheda elettronica, trasformandoli in un segnale TTL 0-5V che controlla la porta logica del MCA: in questo modo è possibile effettuare la soppressione Compton eliminando dallo spettro gli eventi in coincidenza. Al fine di assicurare tale coincidenza tra impulsi riferiti a eventi che vengono rivelati simultaneamente dai due cristalli, una linea di ritardo è stata aggiunta al canale interno. L'intera fase di progettazione è stata realizzata utilizzando il software Altium De-

signer V.10.

La seconda parte del progetto ha riguardato il debug delle schede elettroniche realizzate e la caratterizzazione dei cristalli scintillatori e del SiPM. Questi test iniziali hanno permesso di regolare tutti i parametri della scheda, ossia le tensioni di threshold, gli offset, i guadagni, la banda passante e il ritardo di tempo, in vista della seconda versione dello strumento dove ogni parte superflua, utile solo ai fini dei test, sarà rimossa. Servendoci di una sorgente radioattiva di ^{137}Cs e utilizzando una dinamica di 5V, abbiamo regolato il sistema in modo da ottenere a valle dello shaping del canale interno impulsi di ampiezza intorno ai 2.5V e una costante di tempo di circa 4μs. Per quel che riguarda il canale esterno, abbiamo scelto una costante di tempo di 2μs ottenendo impulsi con un fronte di salita più veloce e un'ampiezza in tensione dello stesso ordine di grandezza. Il ritardo di tempo necessario per garantire la coincidenza è stato fissato a $400ns$.

Infine, è stata testata l'efficienza della soppressione Compton con il nuovo assetto elettronico. Attraverso queste misure si sono potuti analizzare tre principali aspetti che possono influenzare in modo considerevole o inficiare i risultati: il livello della tensione di threshold sul canale esterno, la posizione della sorgente (sopra, sotto, a lato) rispetto al rivelatore, la geometria e le dimensioni degli scintillatori. Modificando i suddetti parametri si è potuto ottimizzare il sistema di rivelazione raggiungendo efficienze di soppressione Compton fino al 40.8%, con la sorgente posta a lato e una threshold intorno ai 230mV. L'efficienza di rivelazione e di conseguenza la soppressione Compton dipendono anche dal volume, dalla forma e dalla qualità della superficie del cristallo esterno all'interfaccia col SiPM: i migliori risultati sono stati ottenuti servendosi del cristallo esterno più nuovo, in termini di fabbricazione, caratterizzato da un corpo cilindrico modellato a tronco di cono nella sua parte finale. Tutte le misure sono state effettuate utilizzando invece come scintillatore interno un cristallo cilindrico di 6x6mm, ottenendo una risoluzione di 9.3%.

Importanti limiti ai risultati sono stati imposti dal rumore elettronico, dalla PDE molto bassa del SiPM (circa il 13%) e dalle superfici deteriorate dei cristalli. Il rapporto segnale/rumore ancora troppo basso e una threshold conseguentemente elevata così come la bassa efficienza intrinseca del SiPM nel rivelare i fotoni di scintillazione del CsI(Tl), hanno impedito di ottenere migliori risultati.

Il miglioramento di questi parametri dovrà essere la base di partenza per il futuro sviluppo dello strumento.

Contents

List of Figures

List of Tables

Chapter 1

Introduction

The increasing importance of radiation physics applied both to medical therapies or diagnostics and many other scientific fields such as material characterizations, has recently led to an augmentation of the international trade in radioisotopes and nuclear materials. Hence, nowadays, accurate controls and detections of this kind of merchandise are required in order to ensure public safety. Moreover, the eventuality of illegal trafficking of nuclear materials makes it necessary to safeguard homeland security.

Given all of these considerations, it is required not only to merely detect the presence of radioactivity but also to identify all transported radioisotopes as well as possible. One of the most powerful and non-invasive detection methods is gamma spectroscopy, which allows the 'ID card' of a nuclear material to obtain. The major limit of gamma spectroscopy concerns the identification of low energy gamma emitters because of the presence of Compton continua, due to the detection of higher energy gamma emissions.

Our goal is to design a detection system which is able to reduce the impact of Compton scattering in order to identify lower energy peaks referred to ^{235}U or ^{239}Pu if present in nuclear merchandises. Many different approaches are available to reach this goal but, as it is a much less expensive and thus more marketable solution, we decided to work on an anti-coincidence dual detector system designed at the CMRP and for which they have obtained a patent. In the following sections we will describe the main features of this system.

1.1 Project aims

The aim of this project was to design and create the first version of an innovative hand-held anticompton spectrometer, under development at the Centre of Medical and Radiation Physics (CMRP), University of Wollongong. The device is based on a dual detector composed of two CsI(Tl) scintillator crystals in a concentric configuration, which are attached to a large area Silicon Photomultiplier array (SiPM). After focusing on SiPM pixels characterisation [30] and on preliminary tests using NIM modules [31], the main goal of this project is to realise the electronics able to read out SiPM signals and to allow both spectroscopy and Compton suppression. Our work aims to optimise all electronic parameters and compontents in view of the definitive version of this device. Another important aspect is to verify the improvements of the results obtained thanks to the new electronics, with respect to the previous work, in terms of both anticompton efficiency and energy resolution.

1.2 Gamma interactions

When you are interested in obtaining energy spectra using a scintillator crystal, only three gamma-rays interactions are really significant: photoelectric absorption, Compton scattering and pair production.

1.2.1 Photoelectric effect

This kind of interaction consists in the complete absorption by an atom of an incident photon and a consequent emission of one of the atomic bound electrons called, in this case, photoelectron. The law of conservation of energy leads to the following formula, which describes the energy distribution in this interaction:

$$E_e = h\nu - E_b$$

Where E_e is the emitted photoelectron energy, $h\nu$ the incident photon energy and E_b the binding energy. When incident photons interact in this way with scintillator atoms, all the energy transferred to the photoelectrons, which have a very short range in high Z materials, is released within the crystal. In the ideal situation where all photons interact with the crystal only by total absorption, the resulting differential energy distribution could be approximated by a delta function centered in hv, shown in Fig.1.1, and photoelectron kinetic energies would have a perfect linear relationship with incident photon energies[13].

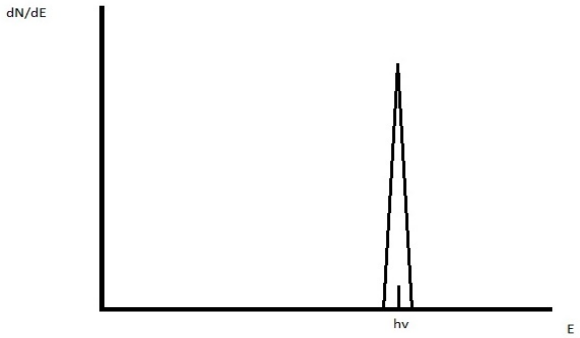

Fig. 1.1: Photoelectric peak [13].

As it is clear from previous considerations, this process determines the ionization of some of the crystal atoms. Its probability of occurrence decreases for increasing photon energies, roughly as E^{-3} (Fig.1.2), with discontinous jumps at those energies corresponding to the electronic shells. As you can see, at energies above the K-shell binding energy, the PE probability, also called PE cross section, strongly decreases and Compton effect becomes predominant[13].

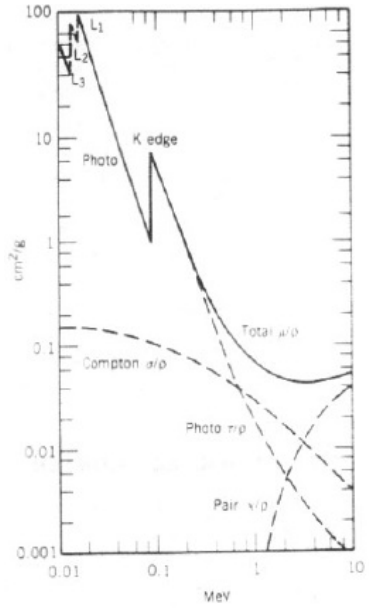

Fig. 1.2: Lead cross section. Example of cross section trend [14].

1.2.2 Compton effect

Compton effect is the name given to the process through which an incident photon scatters with an atomic electron, which is treated as a nearly free electron. This interaction results in a less energetic photon and a scattered electron with a kinetic energy equal to the energy lost by the incident photon.

Fig. 1.3: Scattering compton event [13].

As it is shown in Fig.1.3, in this case the energy distribution depends also on the geometry of the collision event and the photon energy after interaction is estimated with the following formula, calculated by applying the laws of conservation of linear momentum and total energy:

$$h\nu' = \frac{h\nu}{1 + \frac{h\nu(1-cos(\theta))}{m_0 c^2}}$$

Where θ is called scattering angle. The scattered photon energy range goes

from the initial energy $h\nu$ for $\theta = 0°$, which corresponds to forward scattering, to a minimum energy for $\theta = 180°$, corresponding to a frontal collision. The Compton effect cross section depends on the incident photon energy as well as on the scattering angle, as shown in the polar plot in Fig.1.4[13].

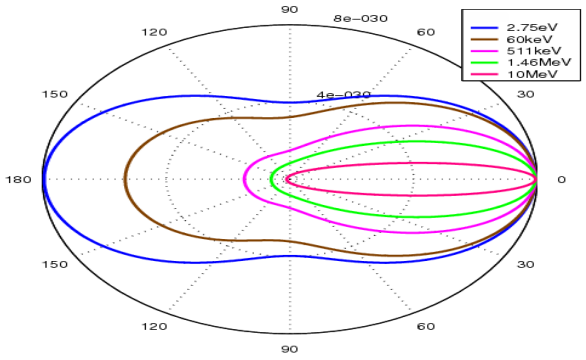

Fig. 1.4: Polar plot of the cross section for Compton scattering from $\theta = 0°$ to $\theta = 180°$ [13].

In case of Compton scattering, the energy of the scattered electron loses its proportionality with that of the incident photon and the effect on the energy spectrum is shown in Fig.1.5.

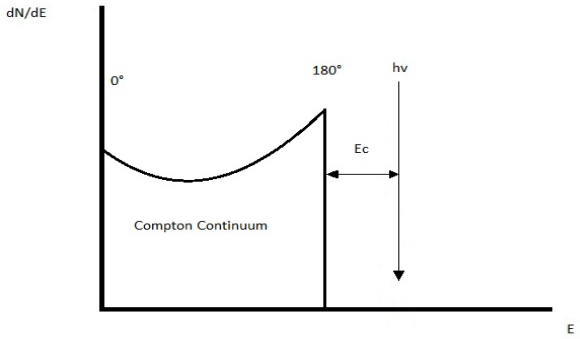

Fig. 1.5: Sketch of Compton continuum [14].

As you can see, the energy released within the crystal depends not only on the initial energy but also on the scattering angle.

1.2.3 Pair production

With the increase of the incident photon energy above 1,022MeV, another interaction, called pair production and in which an electron-positron pair is created, becomes energetically possible. The existence of antiparticles like positrons is justified by the quantistic theory, according to which $E^2 = (mc^2)^2 + (pc)^2$, where negative energy levels are also accepted. Negative and positive energy levels for each kind of particle are separated by an energy gap equal to twice the particle rest energy. If we consider electrons, whose invariant mass is equal to 0,511MeV, it is clear why at least a 1,022MeV photon is necessary to create a positron-electron pair. If the photon has an energy larger than 1,022MeV, the energy distribution follows this formula:

$$h\nu = E_e + E_p + 2m_0c^2$$

Here we can notice that the energy is equally shared between the two resultant particles, as their masses are equivalent. On the energy spectrum, this interaction appears as a peak at $hv - 2m_0c^2$[13].

1.3 CsI(Tl) scintillator crystals

Scintillator crystals are inorganic materials able to emit photons of a specific energy when radiations interact with them. This mechanism is inherent in the crystalline structure and rises to the band distribution of the electronic energy states. In a pure crystal, between the *valence band*, i.e. the lower band filled by the electrons bound in the crystal lattice, and the *conduction band*, i.e. the upper band where electrons can move freely, there is a *forbidden energy gap* where no electronic energy states are permitted[13].

In order to obtain a scintillator crystal, some impurities, called *activators*, are deliberately added to the crystal and new energy states, called *luminescence centers*, are created within the forbidden band. Electrons can be de-excited to the valence band emitting photons which are the result of the scintillation process: the electrons excited by an incident radiation are trapped by the luminescence centers and then de-excite to the valence band. The choice of different materials, activators or concentrations determines the characteristics of the different scintillator crystals.

For our project, we used CsI(Tl) crystals, alkali halide scintillators with Thallium as the activator element, which is characterised by a large gamma-ray absorption coefficient per unit size and good malleability compared to NaI(Tl), allowing various shapes to be obtained without fracturing. Compared to the NaI(Tl), the emitted photon wavelength (550nm) is such that it makes CsI(Tl) inappropriate to match with the response of PMTs. However, the scintillation yield could actually be higher, roughly 65photons/keV, if using photodiodes or SiPMs with extended response in lower energy regions. The decay time is one of the slowest among the most popular scintillator crystals and it has two components with different branching ratio: $0,68\mu$s with a probability of 64% and $3,34\mu$s with a probability of 36% [13].

1.4 Silicon PhotoMultipliers

As we mentioned above, SiPMs represent an interesting solution for the detection of low energy photons emitted by CsI(Tl) crystals. Moreover the high quantum efficiency around 80%, the great multiplication factor around 10^6, the ability to operate at low bias voltages of approximately 30V, their time resolution and sizes make them the principal competitors of PMTs in future applications[15]. This device consists in a matrix of pixels in which there are thousands of passive-quenched Geiger-mode avalanche photodiodes (GM-APDs) connected in parallel to each other. In our project, we use a SensL 4x4 pixels array with 3640 microcells (GM-APDs) in each pixel(Fig.1.6).

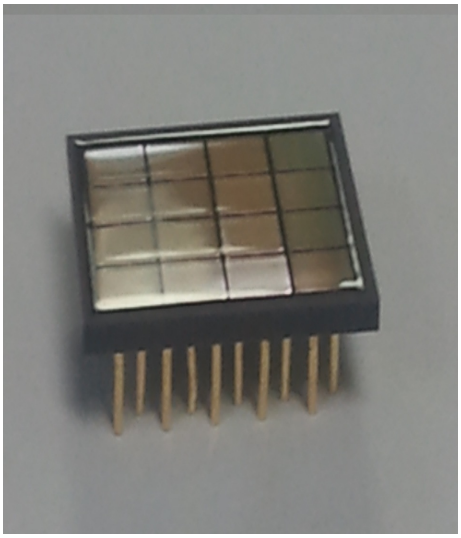

Fig. 1.6: SensL SiPM: $3x3mm^2$ pixel, 4x4 pixels array.

In Fig.1.7 you can see an example of a microcell with a p-type silicon substrate and a p-type layer above which is the active thickness, completely depleted of charge carriers at the operating voltage. Then the dielectric layers on the silicon surface are designed to increase the PDE (photon detection efficiency) for wavelengths around 420/450nm [16].

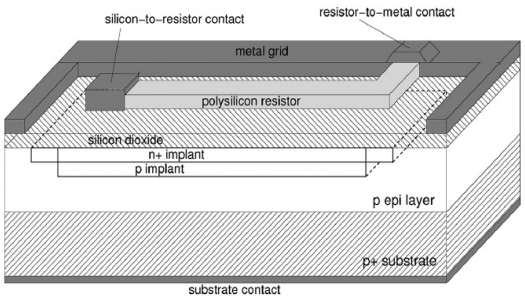

Fig. 1.7: Sketch of a microcell forming the SiPM.

In order to reach gain values of $10^6/10^7$ APDs have to operate at a bias voltage above the breakdown voltage, thus generating a strong electric field in the p-layer. The electrons liberated by the incident photons are accelerated and, reaching great kinetic energy values, they can trigger an avalanche breakdown. During this avalanche breakdown the electric field drops and the V_{bias} decreases under the breakdown voltage, arresting multiplication and allowing the current to spread through the pixel quenching resistence.

Some important goals towards the realisation of reliable SiPMs need to be achieved such as the reduction of the dark current quoted around $1MHz/mm^2$, the temperature instability which can result in a decrease of the V_{BD} of roughly 76mV/°C and the number of photoelectrons (fired pixels) for each incident photon.

The first drawback limits the size of the pixel which in our case is a $3x3mm^2$ square while the second one could cause a variation of the gain which sometimes makes a stabilisation of the detector response necessary by means of a temperature control[17]. In Fig.1.8, it is shown a typical single photoelectron spectrum where peaks, in this case, reveal an excellent single photoelectron resolution of the tested device[18].

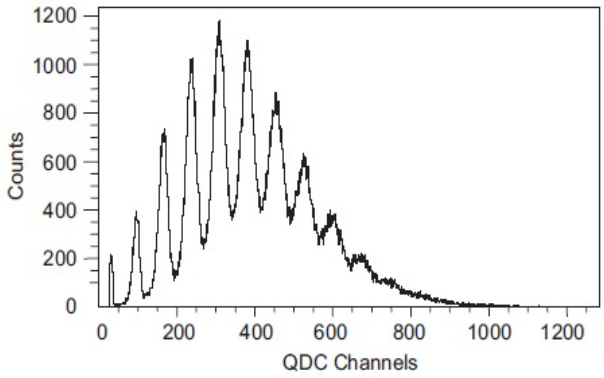

Fig. 1.8: SiPM single photoelectron spectrum measured with a pulsed low-light-level LED at 33.5V[18].

In our project, the dark current is a negligible factor, therefore we can ignore it. We do not approach the problem of temperature dependence in this project, limitating our studies to room temperature, but it will have to be solved given that we are designing a device which will operate in the field supposedly from -20°C to +50°C or even higher. For what concerns the third issue, this could cause a signal distortion as we will explain later. In the first part of our work, *Preliminary steps*, we will be especially interested in ensuring that all 16 pixels have the same behavior in order to understand how we can treat and control them.

1.5 Compton suppression

In the first section we explained how the Compton continuum grows in the energy spectrum due to those scattered photons which escape the scintillator crystal. In this case the incident photons only release a part of their initial energy and this can hide lower energy peaks in the same energy range as shown in Fig.1.9.

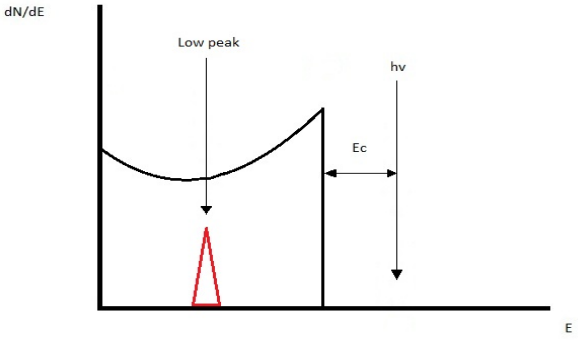

Fig. 1.9: Compton continuum masking the PE peak of a lower energy photon.

Our goal is to suppress the Compton continuum in order to bring out the hidden PE peaks that are of primary interest. In order to reach this goal we will use an anticompton system which includes two scintillator crystals: a small inner crystal which is the actual detector measuring the energy spectrum and an outer crystal surrounding the first one whose task is to detect scattered photons which escape the inner detector. The CMRP obtained a patent on this dual detector design in the Chinese and the US trades.

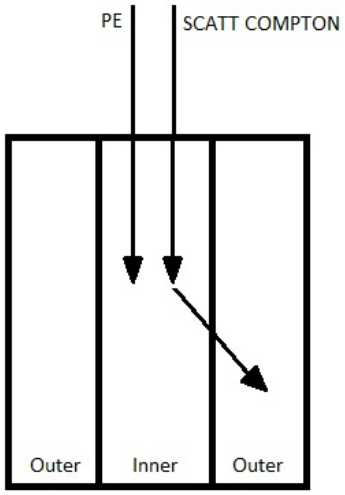

Fig. 1.10: Sketch of the axial section of dual Compton suppression detector. PE and Compton scattering events are presented.

These two detectors are linked to an electronic signal processing stage which produces a gated signal from the outer detector which in turn acts in anti-coincidence with the primary one. This system allows us to remove from the spectrum the signal coming from the inner detector when it is simultaneous with that from the outer one.

Obviously, simultaneity in this case means that the two events occur within a fixed delay time and they are considered to be coincident by the signal processor. Because of this and as the output signal from the outer crystal is always the same gated pulse, many parasite events such as random coincidences can occur distorting real results.

It could happen that two interactions which are not due to compton scattering occur simoultaneously both in the inner and outer detector. In this situation the electronic system is not able to distinguish between true and false events and so random coincidences imply the deletion of true events from the energy spectrum. Random coincidences can be influenced by various factors concerning the outer detector: high count rates, electronic noise peaks or geometry. In particular, a basic contradiction in the outer detector design has to be highlighted: in order to obtain a good Compton suppression system a large volume scintillator crystal with a high counting efficiency is chosen to maximize the probability of detection of Compton scattered photons escaped from the inner crystal, but these same factors increase the probability of random coincidences. In the detector design this issue implies that a good compromise has to be found.

Chapter 2

Literature Review

2.1 Handheld gamma detectors

The aim of this project was to design an innovative handheld anti-Compton suppression gamma spectrometer. In order to do so, a literature review was undertaken considering all possible recent developments of portable probes able to identify radioisotopes emitting radiations in different energy ranges and based on different technologies or physical principles.

In 2006 the American National Standards Institute, jointly with the National Committee on Radiation Instrumentation, published a report specifying all general requirements and test procedures for handheld instruments used for radionuclides identification[12]. In order to be able to identify radionuclides, to measure exposure rate or detect neutron sources in all environmental conditions, this kind of devices must have certain radiation response requirements and electrical, mechanical and environmental requirements. Response time, full-energy-peak efficiency, alarms, false identification, external interferences (surrounding materials, magnetic fields, temperature), hardness, these are just a few important parameters and tests which are analysed in-depth in paper [12].

Based on this standard, many solutions have been commercialised and many others have been developed in various research centres around the world. Generally, the development of this kind of devices is required to determine potential sources of undeclared nuclear materials. Conventional gamma spectrometry, as a non-destructive analytical method, is widely used for this purpose.

Gamma spectroscopy can be realised using scintillator crystals coupled with PMTs, PIN Diodes or SiPMs and solid state semiconductor detectors, with different advantages and disadvantages regarding spectrum resolutions, energy ranges, dimension, cost and power requirements.

The performance of a radioisotope identification device (RID) is determined evaluating two most critical components which are the spectral gamma detectors and associated electronics and the identification software [13]. Each device in the following pages, using different detectors and supports, is compared to the other on different characteristics and peculiarities.

The first device we want to present here is an interesting solution developed in 2009 by the Korea Atomic Energy Research Institute which studied the coupling

between a 11x11x21mm^3 CsI(Tl) scintillator crystal and a PIN diode (Hamamatsu 3590-08) realising a portable device. It is able to obtain high energy resolution values between 7.9% and 4.9% respectively referred to 662keV and 1332 keV (^{137}Cs and ^{60}Co energy peaks) and it is characterised by a very compact design as it is shown in Fig.2.1 [2].

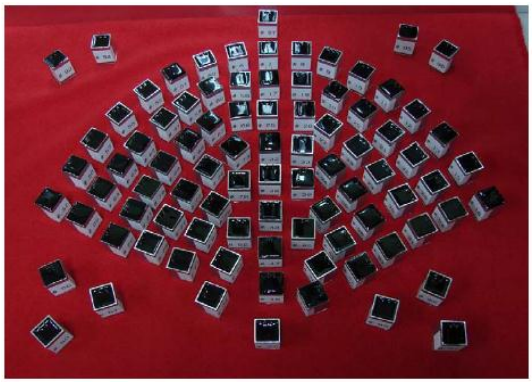

Fig. 2.1: The fabricated CsI(Tl)/PIN diode sensors [2].

The company, Polimaster has commercialised the PM1401K portable gamma detector using CsI(Tl) as scintillator crystal. This device is also able to detect and locate alpha and beta surface contaminations as well as neutron radiation sources including nuclear weapon materials, reaching very good levels of sensitivity (200 $s^{-1}/[\mu Sv/h]$). In fact, this device features three built-in radiation detectors: besides the CsI(Tl) crystal, a Geiger-Muller based detector and a ^{3}He neutron detector are included respectively to measure alpha and beta flux density in the energy range between 0.015Mev and 15Mev and to detect neutrons in the energy range between 0.025MeV and 14MeV (Fig.2.2).

Fig. 2.2: Combined block to measure DER of photon radiations and both alpha and beta flux densities (1); Photon filter which ensures measurements of DER Hp(10); Neutron radiation detector (3); Gamma radiation detector (4) [3].

Through the GM-counter is also possible to evaluate dose rate in the range (DER) between 0.1μSv/h and 100mSv/h[3].

CsI(Tl) was used by Smiths Detection as well in their handheld radiation detector Radseeker, specifically designed to meet the U.S. Department of Homeland Security requirements aiming to identify hazardous nuclear materials. Actually this device was designed in both CsI(Tl) and LBr3 configurations. It has a good energy range between 25keV and 3MeV, high sensitivity levels, alarms indicating gamma/neutron radiations and automatic energy stabilization[4]. During recent years other companies and centres of research have developed devices based on NaI(Tl) scintillator crystals, to the detriment of the stable parameters offered by CsI(Tl) which do not need any calibration source build in or calibration procedure for dose rate measurements. Although CsI(Tl) crystals are cheaper and much less hygroscopic so they do not easily deteriorate and they do not need any casing. Finally, their structural features permit to resist to mechanical and thermal shocks and to be deformed without fractures.

For example, ATOMTEX commercialized the AT6102 Spectrometer using a 40x40mm NaI(Tl) cylindrical crystal coupled with a Geiger-Muller tube and two proportional neutron 3He Counter, reaching sensitivity values higher than those cited above and relative energy resolutions lower than 7.5% at 662keV. Although it assures rapid responses in identifying different radioisotopes such as ^{137}Cs or ^{252}Cf and it can be used not only in environmental or medical fields but also in nuclear applications[5]. Polimaster has also developed a NaI(Tl) based device (PM1410) which permits detection and localization of the source, quick measurements of dose rate even in presence of shield or containers due to have three built-in detectors of different types, similar to Polimaster's PM1401K but using a different scintillator crystal, and to an implemented algorithm of reverse recalculation considering statistical interaction processes between radiation and shielding materials[6]. In 2010, the Radiation Protection Bureau of Health in Canada published a paper[1], concerning the development of a NaI(Tl) based system, to establish a methodology that enables rapid identification of uranium enrichments through gamma-gamma coincidence. In fact, this method allows elimination of all the interferences that prevent uranium identification. This system was realised using two 15.24x17.78cm NaI(Tl) crystals separated 2cm and coupled with two PMTs and positioning the sample in the middle of the two scintillators.

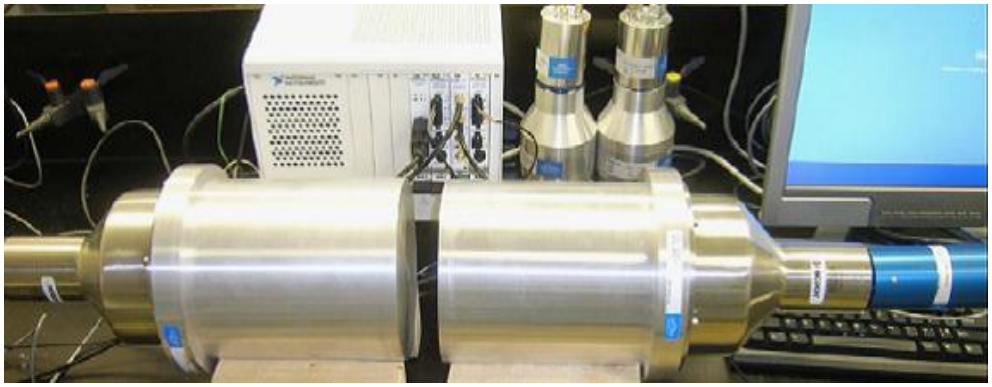

Fig. 2.3: Full system with NaI(Tl) detectors, PMTs and power supply [1].

Orientation and small distance between the detectors provide a large geometry efficiency and maximum cross-talk probability, resulting from coincident backscatter of the ^{235}U 185.7keV gamma ray. So detectors must have a diameter enough big to catch photons scattered from the opposite. Relative energy resolutions of about 7.5% at 662keV has been achieved with samples of different enrichment values and it is shown that gamma-gamma coincidence spectra allows uranium identification and isotope quantification[1]. CsI(Tl) and NaI(Tl) are often chosen as scintillator materials due to their features and costs, but nowadays many other materials are experimented to improve efficiency. LaBr3, for example, offers energy resolution values competitive with semiconductor detectors, room temperature operation and very fast timing. A project supported by the NASA APRA in 2010 reached its goal by developing a handheld detector for space applications using a 6x6x10mm^3 LaBr3 crystal and a Hamamatsu SiPM as light collector, as shown in Fig.2.4, and obtaining energy resolutions under 7.2% at 662keV and rapid responses[7].

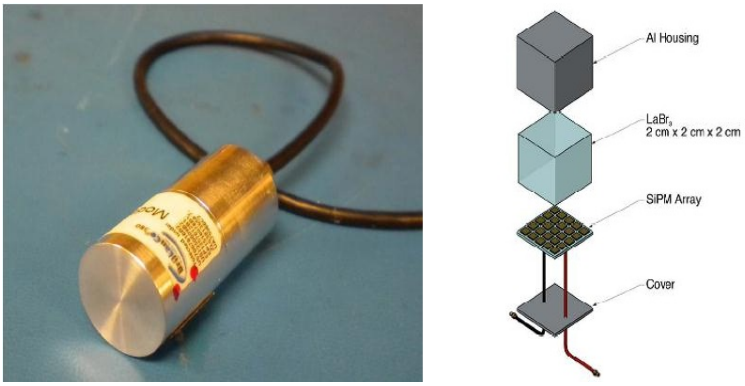

Fig. 2.4: LaBr3/SiPM detector fabricated by saint gobain and planned 1" LaBr3 detector read out by an array of SiPMs [7].

Instead of using scintillator crystals, it is possible to realise gamma spectroscopy with semiconductor materials which continue to progress in terms of quality and cost. Cadmium Zinc Telluride (CZT) detectors are the most commonly used as they allow detection with excellent spatial and in addition to energy resolutions and in addition fast responses, which are required features in the field of Homeland Security applications[9]. Washington University in St. Louis, in addition to others, worked on a large-volume CZT device (0.5x3.9x3.9cm^3) to combine typical semiconductor's high performances with a reduced number of readout channels. Testing their device they achieved very high energy resolutions up to 3% FWHM[8]. In 2011 a new CZT based detector, the PorGamRays Spectrometer, able to provide spectroscopic and positional information was developed by the PorGamRays Collaboration, exploiting a Compton Imaging method using six thin (2mm) CZT films[9]. The Pacific Northwest National Laboratory in 2007 published an article about the development of an innovating handheld radioisotope identifier named GammaTracker utilising two pixelated CZT 3x3 arrays of 2.25cm^3. In the simulations and the measurements presented in the paper, it is shown that GammaTracker is competitive with HPGe detectors in terms of efficiency and sensitivity while this is not the case concerning

energy resolution. It is for this reason that HPGe is usually preferred for spectrometry.

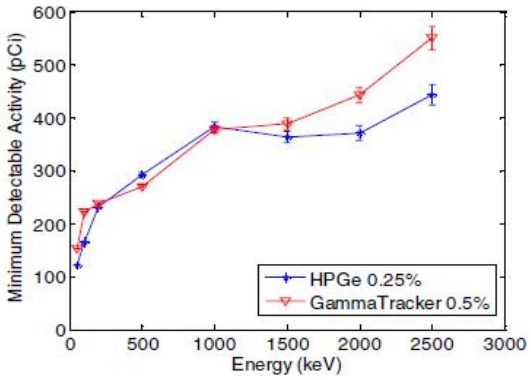

Fig. 2.5: Minimum detectable activities for 1-minute acquisition of GammaTracker at 0.5%FWHM energy resolution and a comparable efficiency HPGe: comparable performances [10].

This kind of detector is also capable of directional sensing, thanks to traditional Compton imaging methods, intersecting a back-projection cone with a given image surface (in this case a sphere surrounding the detector). A method considering the two intersection points between the backprojection cones and the image sphere has been developed and these point are plotted on a 2D image Fig.2.6.

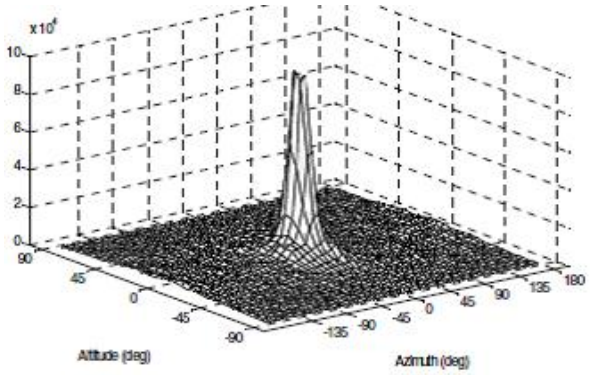

Fig. 2.6: Image of 662keV point source with no background [10].

The results showed that it is possible to achieve energy resolutions of about 20/30% and imaging resolutions around 20%[10]. Another method to identify nuclear isotopes was requested by US nuclear facilities, in order to improve safeguards against special nuclear materials or weapons. One of these systems, called Network-Oriented Radiation Monitoring System (NORMS), was developed at the Idaho National Laboratory (INL) in 2008. It is composed by two 0.5"x1.2" Li6 and Li7 detectors for simultaneous detection of respectively neutron and gamma-rays radiation fields. These two crystals are coupled with two Hamamatsu Photomultipliers,

as shown in Fig.2.7, whose high power supply is provided through a small Cockroft-Walton circuit.

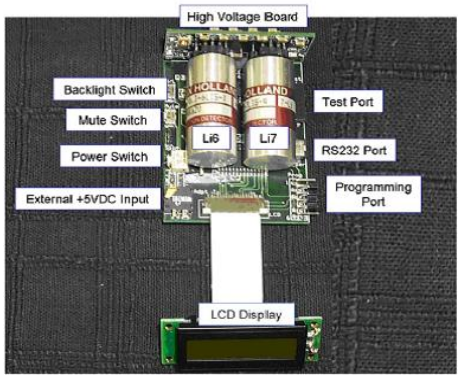

Fig. 2.7: Detection system layout [11].

The system focus is on modular functionality, interactivity, small dimensions and high sensitivity which can achieve 0.1μSv/h and allow detection of small amounts of shielded plutonium, a very important feature in the field of Homeland Security. All data can be transferred to a central facility via direct connection or wireless connection. An external interface board (Fig.2.8) was designed to allow connection to a remote PC through a 900 MHz wireless transceiver. This provide a "transparent" link between the device and the remote station up to 125ft away within a building and could be also set to act as a member of a large distributed group of detection devices placed at strategic choke points in nuclear storage facilities.

Fig. 2.8: RF and interface board [11].

NORMS, thanks to its network capability, is an autonomous and secure method for tracking radioactive materials within a secure environment, already used in other INL applications concerning explosive detection systems[11].

2.2 Compton suppression systems

In this section we are interested in focusing on some Compton suppression systems which have been developed in the recent years. The concept of Compton suppression, developed since the '70s by researchers thanks to emerging technologies which used different materials like scintillator crystals (NaI(Tl)) or semiconductor detectors (HPGe)[19], has seen many progress especially in the last twenty years. In 2000 Riedel and his research group developed an anti-Compton device, made of a HPGe detector surrounded by NaI crystals, in order to reach high sensitivity levels in the detection of radioactive trace elements via NAA. The sample is placed within the detector ring and all the parts (the NaI ring and plug, and the HPGe) are read out by different photomultipliers. Then the output signals, if set in anticoincidence, can strongly reduce the Compton continuum reaching a suppression factor of 16, as it is clearly shown in Fig.2.9[20].

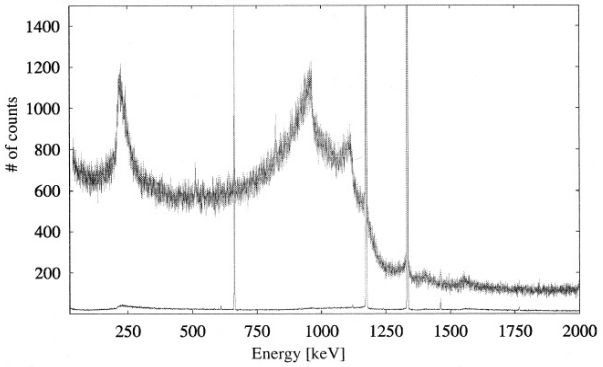

Fig. 2.9: ^{60}Co source measurement: the upper line is without any anticoincidences the lower line is with the NaI(Tl) in anticoincidence[20].

An anti-Compton device would be ideally perfect if the outer detector completely surrounded the inner one covering all possible directions and trajectory of scattered gamma rays[21]. This goal is unreachable for two simple structural reasons concerning the need to allow on one side the incident radiation to directly interact with the primary detector and on the other the contact between this one and the read out system.

At INL, CZT and $LaCl_3$ Compton-suppressed detectors were designed and realised reaching factors of 3.7 to 4.0 for a ^{137}Cs spectrum. These kind of materials have been chosen as primary probes because of their great energy resolutions and high efficiency. On the contrary, as we said in the previous considerations, the veto detector do not need to be a high-resolution but rather a high-efficiency material for photon detection[22]. For this reason BGO or NaI crystals are commonly used and in this case the second one was used obtaining results presented in Fig.2.10.

This technique, which is really useful to detect and identify low energy peaks of radionuclides of primary interest, could lead to underestimate the activities of these radioisotopes. In order to correctly quantify activities, coincidence-summing corrections are suggested to be applied[23], comparing the non-suppression and the

Detector	Type	P / C	Factor	P_A / T_A	Factor
CZT	Unsupp	1.48	4.00	0.18	2.30
	Supp	5.90		0.41	
$LaCl_3$	Unsupp	2.59	3.70	0.19	2.32
	Supp	9.50		0.44	

Fig. 2.10: Results for both the CZT and $LaCl_3$ detectors for the 662keV peak[22].

suppression spectra and estimating correction factors via verified equations.

In the next section we will explain the similar technique applied to our detection system both on the side of the detector geometry and on the side of the electronic design.

2.3 SiPMs read-out systems

In different scientific fields a small size and high gain photo-detector is desired to realise compact systems. For example, for PET systems which are currently based on PMTs and limited in terms of spatial and timing resolution, it would be a desirable solution to employ Silicon Photomultipiers which guarantee compactness, high-resolution and sensitivity[24]. The primary issue of this kind of systems is its cost and cost reduction is the main goal of current research. It was shown that SiPMs, used as read-out devices for scintillator crystals like LSO or LYSO in PET systems, can reach single photoelectron resolutions of 16%, multiplication factors of $10^5/10^6$ [24], energy resolutions of 22% in terms of FWHM at 511keV and a mean PDE around 12% (improvable by using structures with better-matched sensitivity in the blue wavelength of LSO/LYSO photons)[25].

These devices could be useful in many other medical and scientific fields like hadron therapy, calorimetry, astronomy as well as space applications[26]: dose monitoring has been tested coupling a $LaBr_3$ crystal with a SiPM and promising results were obtained such as energy resolution of 7% FWHM at 511keV, spatial resolution around 1.2mm FWHM and timing resolution of approximately 1ns FWHM [27].

APDs arrays, on which the technology of SiPMs is based, are also coupled with scintillator crystals and employed in γ/X-ray spectrometry. Mean energy resolution around 8% at 662keV has been achieved using a CsI(Tl) scintillator and, as expected, cross talk and light sharing are presented as disadvantages which can distort results[28].

The characterisation of MPPC arrays has been done by the National Centre for Nuclear Research in Poland[29], comparing results which were obtained using four different scintillators (CsI(Tl), LSO:Ce(Ca); $LaBr_3$, BGO) of different sizes. This study clearly explains the dependence of MPPC features from various factors. As an example, it shows how the V_{bias} applied to the MPPC has to be chosen finding the best compromise between the desirable increase of the PHE and the worsening of

the energy resolution. In the same way, the size of the crystals, the number of pixels or the optical matching influence light collection, the linearity of the responses and the energy resolution[29].

All these considerations must be taken into account to optimise measurement systems.

2.4 Previous work at CMRP

Between 2007 and 2011 the Centre for Medical Radiation Physics of the University of Wollongong started working in this field. The aims of these first studies were the characterisation of an innovative hand-held Compton suppression dual detector using PIN photodiodes to read out the inner scintillator and the comparison of these results with those obtained with the same system connected to a SiPM array. At first, a PMT was used to collect light from the outer scintillator but then they started investigating an improved Compton suppression system using a SiPM as read out system for both the outer and the inner one. All these measurements were done changing the size and the shape of both the crystals trying to find the optimum.

First of all, the new SiPM was characterised by focusing in particular on the three main issues which affect its performance: the dark current, the internal gain and the dark rate[30]. All these parameters change with temperature and V_{bias} and their dependence on each other has been accurately analysed. As it is shown in Fig.2.11 there is a linear correlation between V_{bias} and temperature. On the contrary the gain, expressed as a function of the dark count (DC) as $G = \frac{I_{leakage}}{DC*q}$ where q is the electronic charge, is not directly related to the temperature. It decreases as a consequence of the increasing V_{bias} (Fig.2.12). The analysis of the dark count rate shows that, in the range of temperature between 290 and 295K, the gain is maximum and the dark count is minimum for different operating breakdown voltage[30].

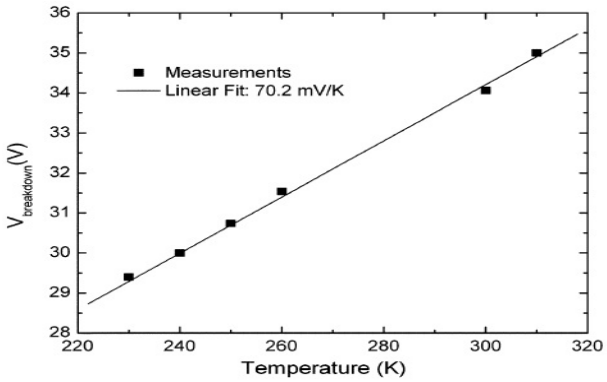

Fig. 2.11: Breakdown voltage as a function of temperature[30].

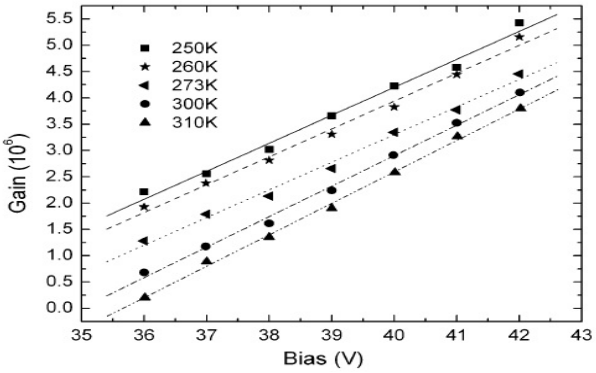

Fig. 2.12: Gain as a function of breakdown voltage[30].

The work proceeded with the measurement of different energetic spectra of various radionuclides using Si photodiodes, showing the inability to resolve photopeaks (Fig.2.13) probably due to the optical coupling and the increase in leakage current over time. The promising characteristics of the PIN photodiodes make them devices which will be able to work in a Compton suppression system like this but some issues need to be solved[31].

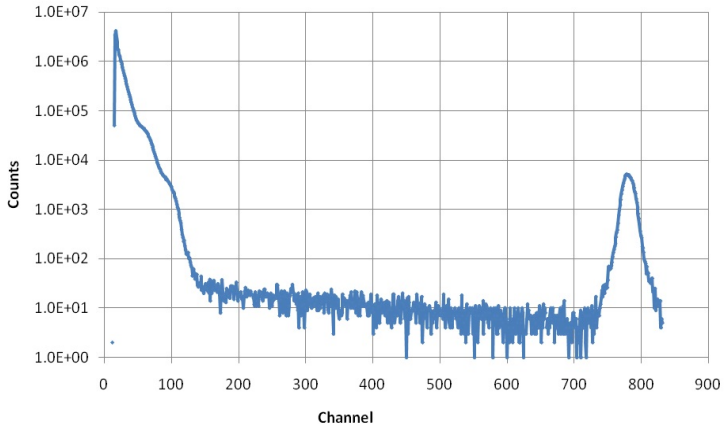

Fig. 2.13: ^{137}Cs gamma spectrum is not resolved. The peak shown at energy 350keV arises from the pulser[31].

Concerning the use of SiPMs, a good but improvable energy resolution around 15% at 511keV (^{22}Na) was achieved and a minimum detectable energy of 80keV was reached with the 12mm inner scintillator which has the smallest amount of light loss.

The Compton suppression study gave good results when the outer detector was coupled with a PMT, clarifying that the increase in sizes of the inner crystal implies an increase in the amount of compton suppression.

Finally, coupling both the detectors to the SiPM, it was found that the minimum detectable energy was higher due to the increased noise and that a Compton suppression around 10% can be achieved, as shown in Fig.2.14 [31].

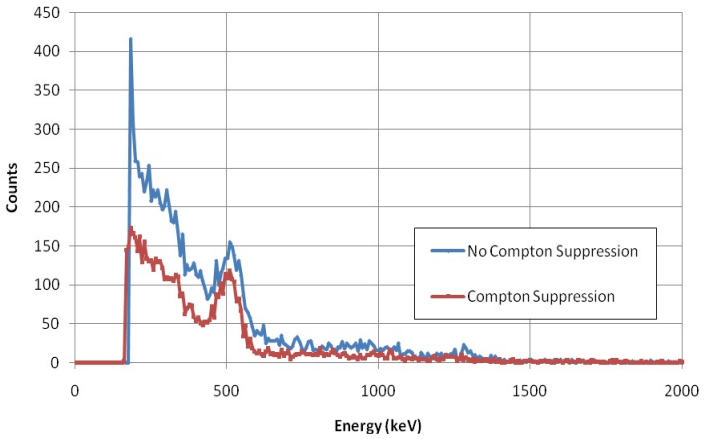

Fig. 2.14: Results of Compton suppression for a ^{22}Na source using a 40x12 Cyl-Con outer detector[31].

All these results were found using NIM modules and with a non-perfect alignment which produces high noise and a higher detectable energy. They can be performed by using a more sofisticated electronic design and more accuracy in the experimental set-up, which is what we intend to do.

Chapter 3

System design

3.1 SiPM and preamplifier board

SensL provided us with two 4x4 pixels Silicon Photomultipliers whose pixels, as shown in Fig.3.1, have a 3x3mm^2 area. The active area of each pixel is roughly 70% of the total area which contains 3640 APDs (35μm^2 each) separated by etched tranches showed in Fig.3.2.

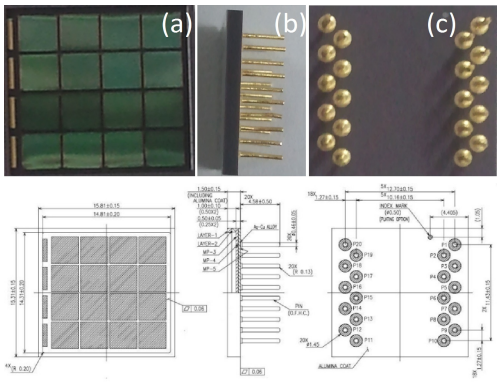

Fig. 3.1: Silicon Photomultiplier sizes and views: top (a), side (b), bottom (c).

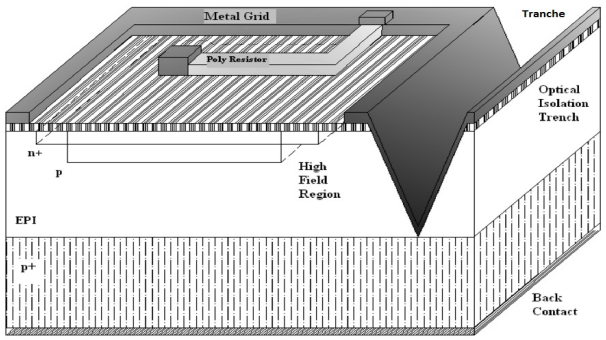

Fig. 3.2: SiPM microcell: view of the tranche which separates adjacent cells.

As we accurately explained in the introduction, each APD is a shallow p-n junction connected to a quenching resistor. The SiPM needs to be powered between 27V and 30V (V_{bias}) and it is characterised by an input current absorption of 50mA maximum.

The company provided us also with a Preamplifier Board where the SiPM is positioned, as shown in Fig.3.3. It consists of four main parts: the SiPM support, the preamplifier part with 16 indipendent channels with differential outputs, the outputs and power interface via a 50-ways FFC on the top layer or via a 80-ways on the bottom layer or via a sherlock connector. The preamplifier board has to be powered by $\pm 3.3V$.

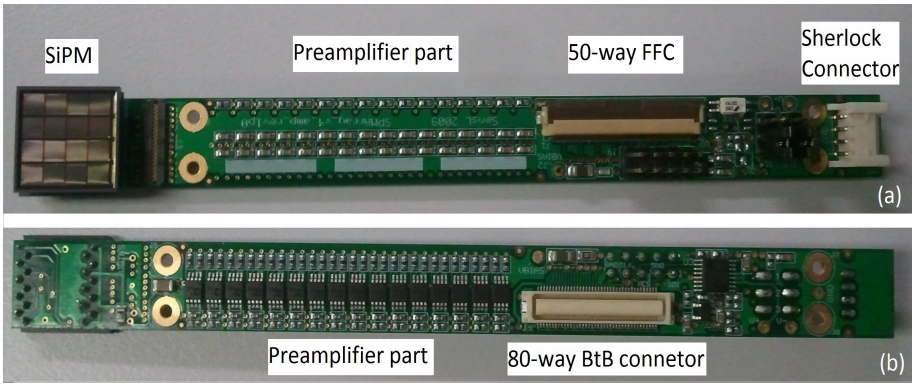

Fig. 3.3: Preamplifier board: top (a) and bottom (b).

For our purposes we can ideally divide the 16 pixels of the Silicon Photomultiplier into two groups: the 4 inner pixels which will be connected to the inner detector and the other 12 pixels, matched with the outer one. Some criticities concerning the geometry of the coupling will be discussed in Par.3.3.

3.2 Scintillators

We had a great variety of crystals which differed in shape and size. Nevertheless, they had some constant parameters due to the fact that their design was based on SiPM dimensions and requirements.

Inner scintillator crystals

As the four inner pixels of the Silicon Photomuplier cover an area of 6x6mm^2, the inner scintillators are designed in such a way that they can match with this internal area of the SiPM.

In theory, the best crystal shape in terms of efficiency and light collection is the cubic one. Evident troubles in the fabrication of a cubic crystal with perfect edges make the cylinder the most used shape to realise efficient scintillator crystals. For this reasons all inner crystals are CsI(Tl) cylinders with different heights but with the same diameter of 6mm, in order to precisely match with the SiPM, as shown in

Fig.3.7. We had three inner scintillators, shown in Fig.3.4: they were 6mm, 9mm and 12mm high and optically isolated on the lateral surface, which will be in contact with the outer crystal, with several layers of teflon tape.

Fig. 3.4: Inner scintillator crystals 12mm, 9mm and 6mm high.

Outer scintillator crystals

For the same reasons we mentioned in the section *Compton suppression*, outer crystals need to be more massive than the inner ones in order to reach good Compton suppression factors. However, the project requirements for a portable probe induced us to limit their size and weight. Moreover the shape of these crystals needed to be designed in such a way that they had interface surfaces able to match the SiPM, which has a 12x12mm^2 area, and such that they could guide the light output to the SiPM. All the outer detectors had a central cylindrical guide with a diameter of 6mm where the inner detector had to be allocated and they consisted in 2 parts: a body and a terminal part. We had three different outer crystals which differed in terms of body, terminal shape and interface surfaces (Fig.3.5 and Tab.3.1).

CRYSTAL	BODY SHAPE	BODY SIZE	TERMINAL	INTERFACE
1	Cylinder	r=40; h=30	Cone	circ; r=12
2	Cylinder	r=40; h=20	Cone	circ; r=12
3	Parallel	l=40; h=20	Pyr	square; l=12

Table 3.1: Table of all main features of outer detectors. Sizes in mm.

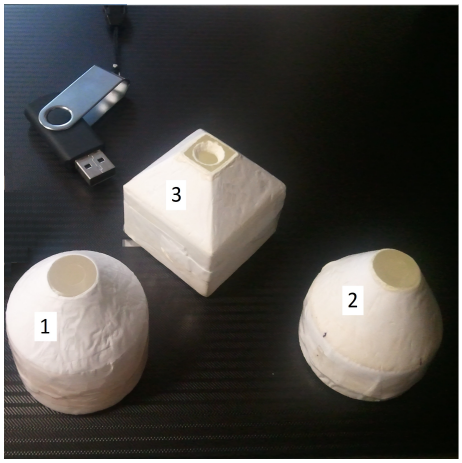

Fig. 3.5: The three outer scintillator crystals with different shape and size.

3.3 Coupling geometry

The coupling between the detectors and the SiPM was optimised by using an optical grease in order to minimise optical reflections at the interface due to the different refractive index. The devices we presented before are coupled as shown in Fig.3.6, where we can notice the conic shape of the terminal part of the detector which works like a light guide, while in Fig.3.7 it is shown how the interface surfaces of the detectors match with the SiPM in all possible cases: the 4 inner pixels of the photomultiplier are supposed to collect information coming from the inner scintillator, while the 12 pixels on the edge are associated to the outer output signals. This situation involves some criticities that we have to solve if we want to obtain good results: the light sharing and the cross talk.

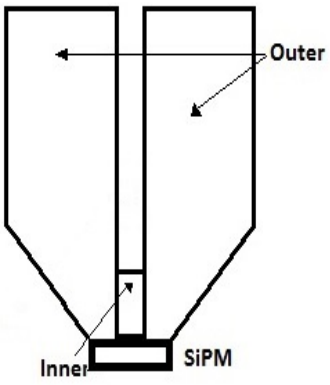

Fig. 3.6: Coupled system: scintillator crystals and SiPM.

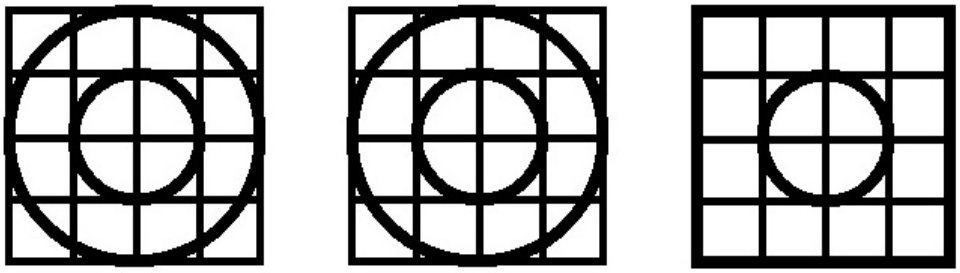

Fig. 3.7: Projection of the outer scintillator interface surfces of the SiPM pixels.

Light sharing and cross talk

The four inner pixel corners we coloured with red in Fig.3.8 are very critical parts in our set-up. In fact, although the four pixels are associated to the inner detector and thus their output current pulses are considered as information coming from it, they receive light from the outer crystal as well, implying distortions in the energy spectrum because of the increased noise. This issue, called *light-sharing*, can be partly solved by placing a reflective paint on the outer scintillator surface in such a way that it covers the red-area between the inner pixels and the outer crystal. However, it is possible to have light-sharing even at the interface between the two crystals wich are in close contact inside the guide. This is the reason why we covered the inner one with some layers of Teflon tape.

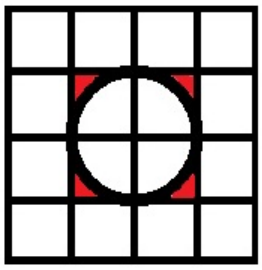

Fig. 3.8: Light-sharing in correspondence with the four inner pixel corners.

Another important issue we have to cosider in this section is the cross-talk in the SiPM. This phenomenon consists of indesired effects produced on some microcells by the adjacent ones and it is partly stopped by the trenches between the cells. The difference between the inner and the outer count rate, which is orders of magnitude lager than the other one, makes this an important disadvatage in terms of noise and resolution in the energy spectrum.

3.4 The electronic design

Concerning the electronics, we based our design on the configuration suggested in 1998 by the nuclear instruments company Canberra. Compton suppression devices do not require fast timing or fast coincidence electronics in order to obtain good results. The very simple and low cost approach system they realised is presented in Fig.3.9 and it gave very good results compared to more sophisticated configurations. In this configuration the signal coming from the inner detector is split into two parts: the first one, for timing analysis, sends the pulse to the coincidence module with the outer detector signal, while the second one sends it to the MCA for energy analysis. Consequently, if the outer and the inner signals arrive simoultaneously to the coincidence module, the signal is not taken into account by the ADC due to the presence of the gate which vetoes the inner pulse. Using a SCA with a lower level above the noise it is prevented that the noise can veto true counts in the spectrum[32].

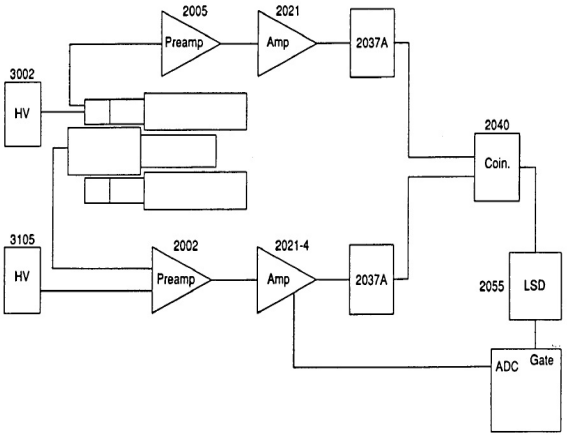

Fig. 3.9: Electronic configuration for a Compton suppression spectrometer with standard timing by Canberra[32].

A simplified sketch of the electronic configuration we decided to realise is shown in Fig.3.10. As the outputs of the 80-way board-to-board connector on the preamplifier board (PB) are differential signals, which implies we have two complementary voltage signals associated to each pixel current pulse, we needed to provide our board with a stage which was able to convert these outputs into single-ended signals. This kind of signal is needed to do spectroscopic studies, so that after the differential-single ended converter we have 16 signals referred to the 16 SiPM pixels. The signals coming from the four inner pixels and those coming from the twelve outer pixels are respectively added (ADDER IN and ADDER OUT) in order to obtain only two output signals, one associated to the inner detector and the other associated to the outer one. Starting from very high frequency pulses, we want to obtain signals with a more suitable waveform for the gate and the MCA analysis, such that both the inner and the outer pulses are shaped through a filter to limit their bandwidth. The Compton suppression is made possible by sending the two signals to the gate, where

the outer signal can veto the inner pulse if the logic level is low. In order to use the outer signal as a veto for timing analysis, we needed a Single Channel Analyser (SCA) to convert pulses into a TTL signal with higher voltage value representing the high logic level and a lower voltage value representing the low logic level. Obviously, as the outer signal passes through the SCA, we needed to delay the inner channel to restore eventual coincidences. If the gate lets the inner shaped pulse pass through it, the latter is sent to the Multi Channel Analyser (MCA) for energy analysis and to record the count in the energy spectrum.

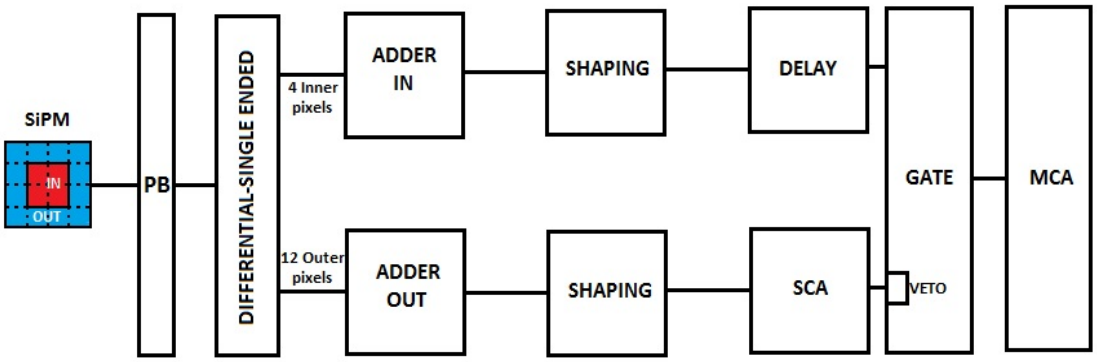

Fig. 3.10: Diagram of the electronic design for the anticompton handheld gamma probe.

Chapter 4

Preliminary steps

4.1 Characterisation of the two SiPMs

Initially, the two SiPM samples were characterised applying different bias voltages to each pixel and monitoring the dark current variations. These measurements were required to define the most high-performance array in order to use it in future experiments.

Instruments and experimental set-up

As we presented in the part concerning SiPMs main features, in standard working conditions a typical reverse voltage of 29.4V is applied to each pixel, approximately 2V over the breakdown voltage, and so we analysed their behavior primarily around this value. The system we used both to provide the bias voltage to and measure current from the samples was made up of three parts: the Keithley 230 Programmable Voltage Source, the Keithley 614 Electrometer and the Keithley 199 System DMM/Scanner. The first one applied a positive voltage to the cathode, the second one linked the anode to the ground potential and it was able to measure current through pixels. The last part just had to convert current values to proportional voltage values. Then all information was sent to a PC through GPIBs, linked to the voltage source and the scanner.

The sample was positioned in a metallic box and accurately locked in order to prevent signal distortions due to incident light on SiPM surface. A LabVIEW interface was used for system control, through adjusting parameters such as voltage, time etc.

Current measurements were taken whilst applying voltages from 0 to 31 Volts with 0.1V steps. The following results were obtained

Results and conclusion

$SiPM_1$

As shown in the graphs below, almost all pixels of the first SiPM present the same behavior except one, which clearly has a breakdown voltage lower than that of the others.

To more precisely evaluate the breakdown voltage mean and standard deviation,

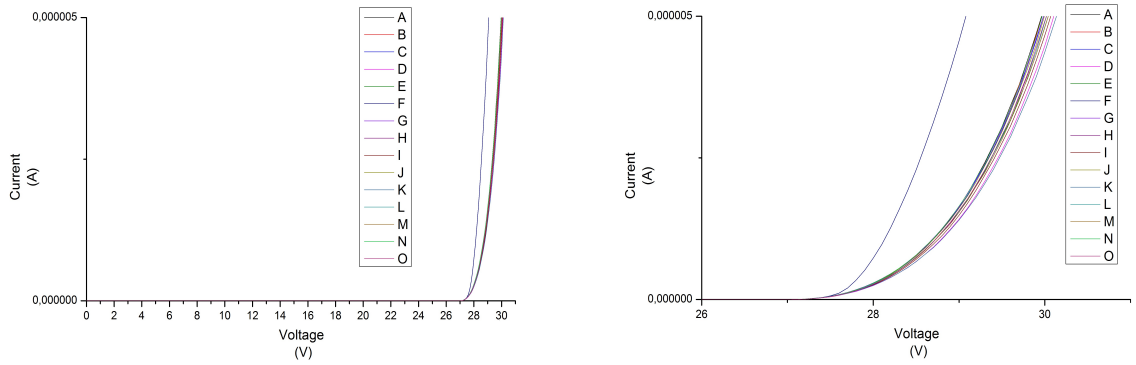

Fig. 4.1: SiPM1: Dark current in ranges 0-31V and 26-30V.

an interpolation technique was used based on the logarithmic scale graph. Fig.4.1 clearly illustrates the point where current begins to increase exponentially.

Through our fitting and interpolation we calculated our parameters as follows:

$\mathbf{V}_{BD}$ **MEAN**	$\mathbf{V}_{BD}$ **STD DEV**
27,03893 V	0,011168 V

Table 4.1: SiPM1: Breakdown voltage mean and standard deviation.

$SiPM_2$

The second sample was characterised using the same method as the first SiPM. The linear and logarithmic scale graphs, focused on the VBD point, are presented below in Fig.4.2.

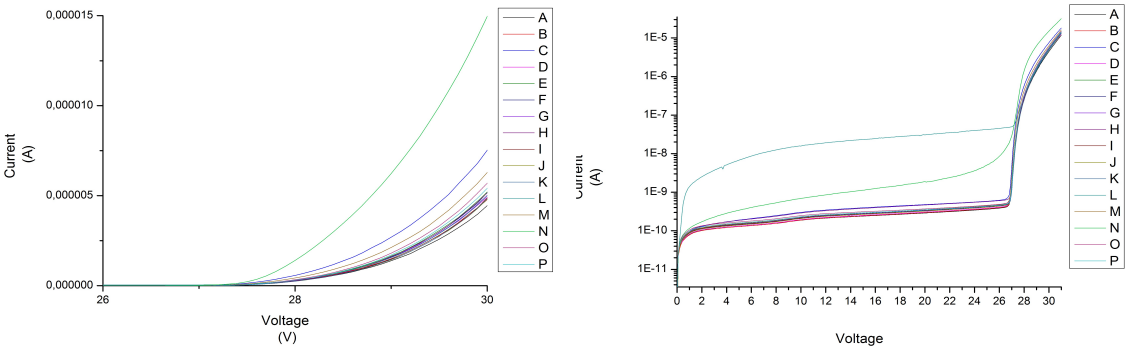

Fig. 4.2: SiPM2: Dark current in ranges 26-30V and logarithmic graph in ranges 0-31V.

The pixels behavior in this sample is less uniform than the previous one. Applying the same interpolation technique and the same parameters the following values for the breakdown voltage mean and standard deviation are evaluated:

V_{BD} MEAN	V_{BD} STD DEV
27,01895 V	0,047767 V

Table 4.2: SiPM2: Breakdown voltage mean and standard deviation.

The standard deviation shows that the variability of the breakdown voltage in the second SiPM is almost five times greater than the first one. This could cause important differences between pixels multiplication factors within the same detector and consequently non-uniform output signals.

Hence, in the following sections we refer to the first SiPM, selected according to previous considerations.

4.2 Characterisation of scintillator crystals

Another important preliminary study before starting measurements was the characterisation of the scintillator crystals we had. We were interested in knowing wich shape and size ensured the best performances in terms of energy resolution and count rate, analysing the FWHM of the PE peak referred to a radiation source.

For our test, as it is a comparison between different crystals, we decided to use a PMT readout system because it allowed to obtain more accurate results. The experimental set-up was made up of a module providing the high voltage (1100V) to the PMT, which was placed in a metal box with the radioactive source and the scintillator, an oscilloscope connected to the shaper (used to set the parameters of the shaping of the signals coming from the PMT) and a MCA which collected all data generating the energy spectrum. The MCA was connected to a PC through a USB-RS232 converter cable in order to display the resulting spectrum.

One of the scintillator crystals surfaces was coupled with the PMT through an optical grease to limit photon reflections at the interface, while the others were covered by an optical reflective material (Teflon tape) to limit the loss of light. For this study a ^{22}Na radioactive source emitting gamma rays at 511keV and 1274.5keV was placed into the metal box and ermetically closed in order to prevent external light from getting in and distorting results.

In Tab.4.3 the results we obtained for the inner scintillators are presented. You can notice that there are no notable differences concerning the energy resolution values, but it is clear that the decrease of the sizes implies an important decrease in terms of count rate. In Fig.4.3 the spectrum collected with the 12mm inner crystal is shown, where the minimum detectable energy is around 60keV. We collected data changing the gain and the shaping time and we found that all parameters were optimised using a gain of 500 and a shaping time of $2\mu s$. All these results are supposed to get worse using a SiPM readout due to the matching with the crystals.

Using the same experimental set up and the same radioactive source ^{22}Na, we compared the outer detectors with a gain of 800 and a shaping time of $2\mu s$. We measured the energy resolution of the three detectors comparing the results with a cylindrical CsI(Tl) scintillator crystal (40x40mm) which was not presented in the previous section. This scintillator was used as a reference for the others thanks to

CRYSTAL	FWHM	COUNTS
6mm	10,8%	5454
9mm	9,8%	8632
12mm	10,2%	10435

Table 4.3: Resolution and data colleted for 11min referred to the 511keV peak.

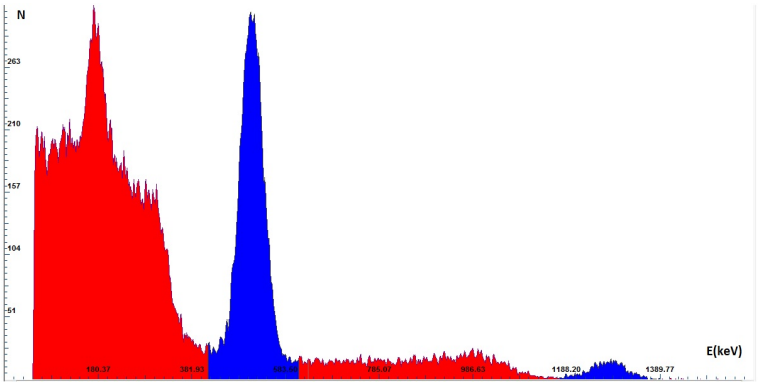

Fig. 4.3: ^{22}Na Energy spectrum measured using the 12mm inner cylindrical detector coupled with a PMT.

its geometry which optimises light collection, energy resolution and count rate. The results we obtained are presented in Tab.4.4:

CRYSTAL	FWHM	COUNTS
Ref	12,1%	33562
1	12,9%	21931
2	13,3%	18862
3	15,9%	31691

Table 4.4: Resolution and data colleted for 5min referred to the 511keV peak.

This table clearly shows that the cylindrical reference scintillator gave the best results in terms of both energy resolution and light output, as expected.

Concerning the conic crystals, which have interface surfaces with the same size, the good energy resolutions (FWHM) are comparable and the small increase could be explained by their different angle. Nevertheless, the conic shape implies a great decrease of the light output because of the reflection on the edge of the cone, while in the cylindrical crystal the light has a direct path. This decrease in light output, respectively of 35% and 44%, represents a clear desadvantage when we use these outer detectors as Compton suppression shields, because many scattered gamma rays may not be vetoed. The energy spectra for this two outer scintillators are compared in Fig.4.4 where the minimum detectable energy is around 75keV.

The square outer detector gave us very good results in terms of light output thanks to its greater surface area and its greater interface area, which makes it

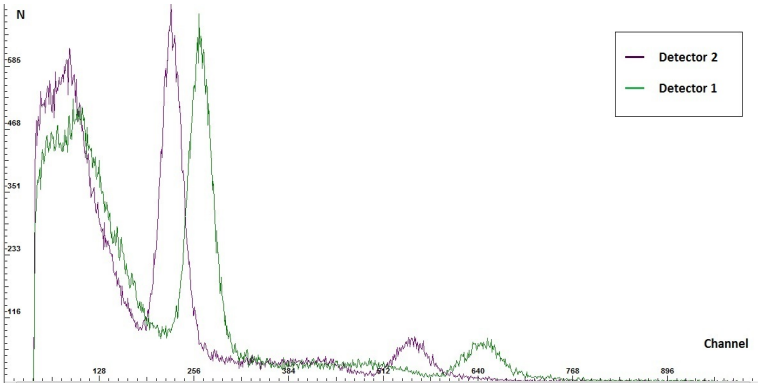

Fig. 4.4: Comparison between the ^{22}Na energy spectrum measured through the two conic detector with two different angles.

a good shield detector for Compton suppression. On the other hand the energy resolution gets worse due to its shape. The energy spectrum measured using this detector is shown in Fig.4.5 where you can remark that the minimum detectable energy is around 120keV.

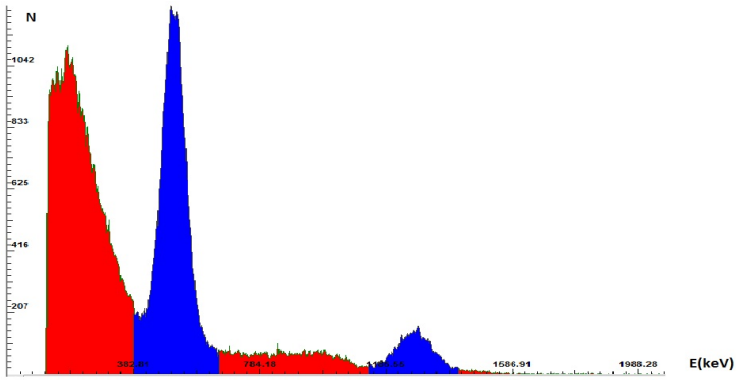

Fig. 4.5: ^{22}Na Energy spectrum measured using the square outer detector.

Chapter 5

Electronic boards layout

After having characterised the main parts constituing the front-end of our detection system, we turned our attention to the developpement of the electronics. To realise a complete and exhaustive system we needed to design two electronic boards for both the power supply and the signal processing. The first design of these two boards have to comply as far as possible with some fundamental requirements:

- Low power consumption.
- Compactness.
- To replace the use of NIM modules (shaping, delay and power supply).
- To allow various delay lines combinations.
- Monitoring of crucial circuit points.

5.1 Signal processing board

Taking into account all these factors, we approached the electronic design starting with the layout of the signal processing board.

First of all we faced the issue of the matching between the preamplifier board provided by SensL and our board. This meant that on one side we had to provide our signal processing board with holes which matched with the holes of the first one, allowing to fix them toghether, and on the other we had to accurately design and place the connection for the 80-way board-to-board connector. Final results are shown in Fig.5.10 at the end of this section. As the outputs from the preamplification board are differential signals, we needed to convert them into single-ended signals in order to do spectroscopic studies. This methode of transmitting electric signals also guarantee some advantages like low cost configurations and the need of fewer wires. The schematics of these two parts, the connector and the differential-to-SingleEnded converter (DSEC) are shown in Fig.5.1, where only one of the sixteen DSECs is presented. The two differential outputs, coming from each pixel through the connector, are respectively sent to the non-inverting and the inverting inputs of the first AD8051 high speed amplifier obtaining an output signal proportional to the photonic flux in the SiPM pixels $\frac{dN}{dt}$. The second stage is required in order to adjust

the offset of our signal, using a trimmer through which we can impose a voltage to the non-inverting input of the second AD8051.

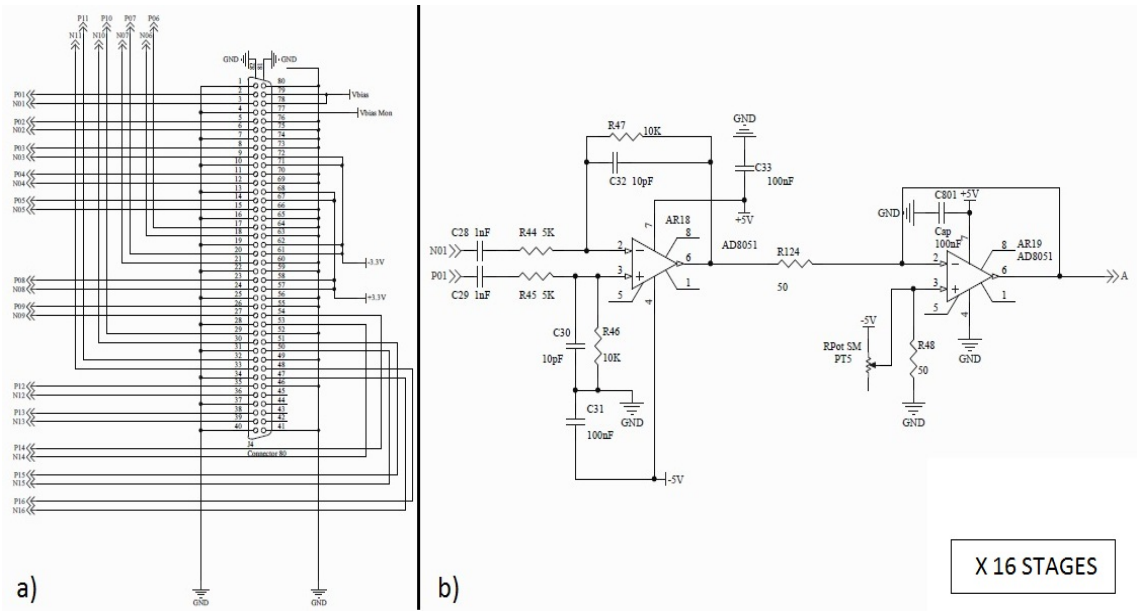

Fig. 5.1: Schematic of the 80-way board-to-board connector (a) and one of the sixteen differential-to-single ended converter (b).

In the following stage, we needed to add the signals coming from the four inner pixels and the twelve outer pixels in order to obtain two pulses respectively associated to the inner and the outer detector as it is shown in Fig.5.2 and Fig.5.3. The OPA656u combines a very wideband and unity-gain stable operational amplifier with a FET-input allowing exceptional performance in high-speed and low-noise applications.

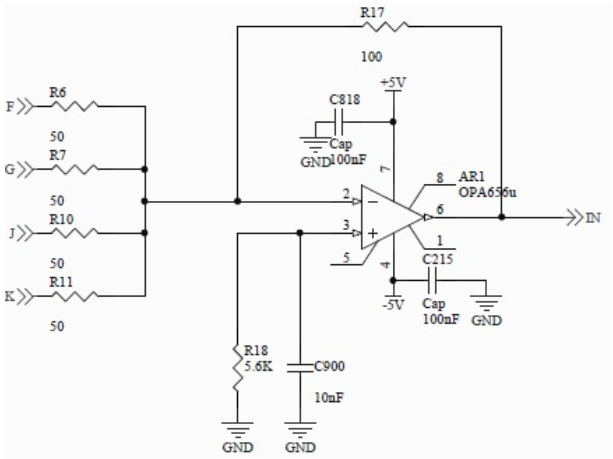

Fig. 5.2: Adder for the four central pixels F,G,J,K.

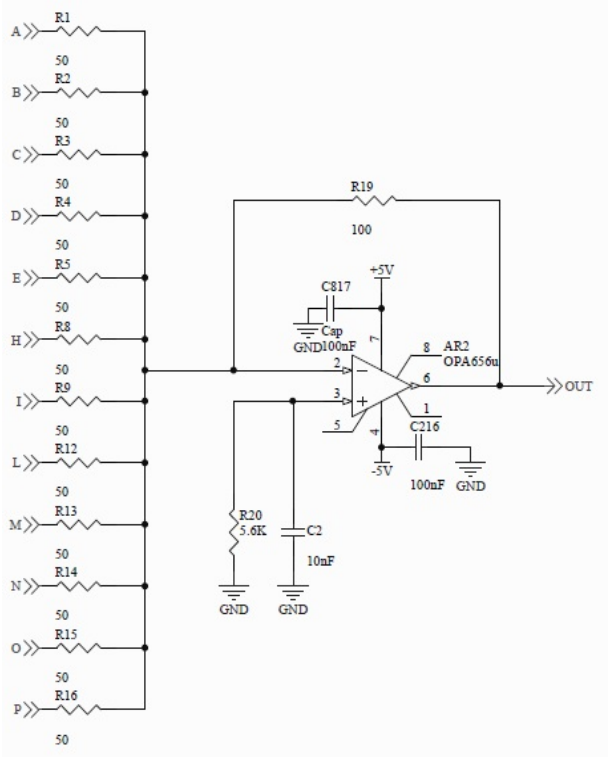

Fig. 5.3: Adder for the twelve pixels on the SiPM's edge A,B,C,D,E,H,I,L,M,N,O,P.

Starting from this moment, the two signals follow different routes because they are used for different purposes.

Concerning the outer signal, which is not used to implement the energy spectrum but only for timing analysis and Compton suppression, it is necessary to limit its the bandwith, through a low-pass filter, shaping the pulse as shown in Fig.5.6. Through an RC-CR network combined with an AD8651 op amp, which allows high-precision and low-distorsion applications, we obtain a larger pulse with a lower bandwidth and a timewidth equal to the sum of the two time constant τ_{RC} and τ_{CR}. The schematic of the shaping system is presented below in Fig.5.4, where the CR derivator is used to avoid overshoots. You can remark here that a voltage reference REF5025, coupled whith an other trimmer, is used to adjust the voltage applied to the non-inverting input of the operational amplifier. This shaped pulse, because of its new timing characteristics, can now be sent to the following Single Channel Analyser (SCA).

The SCA has the task of converting the shaped pulse into a logic low-active signal with a higher voltage value (5V) representing the binary digit of 0 and a lower voltage value, in this case the ground voltage, representing the binary digit of 1 (Fig.5.5). This result is obtained by fixing a threshold voltage at the non-inverting input of the comparator (MAX941) which gives as output a TTL signal with $V_{out} = 0V$ when $V_{in} \geq V_{th}$ and $V_{out} = 5V$ when $V_{in} \leq V_{th}$. This logic signal is sent to the gate in the MCA to veto the inner pulse if $V_{out} = 0$ as it is shown in Fig.5.9 which we will analyse later in this section.

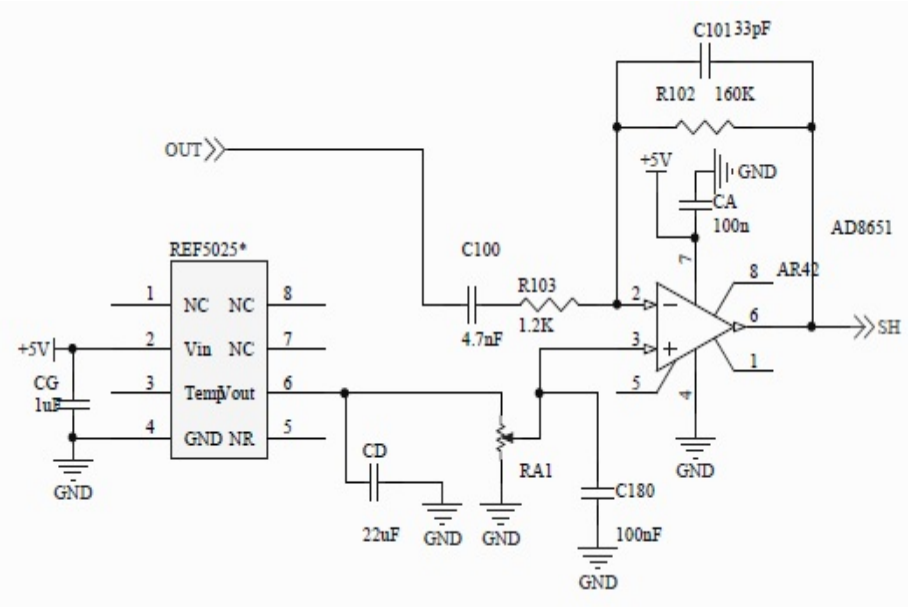

Fig. 5.4: Schematic of the shaping stage of the outer signal.

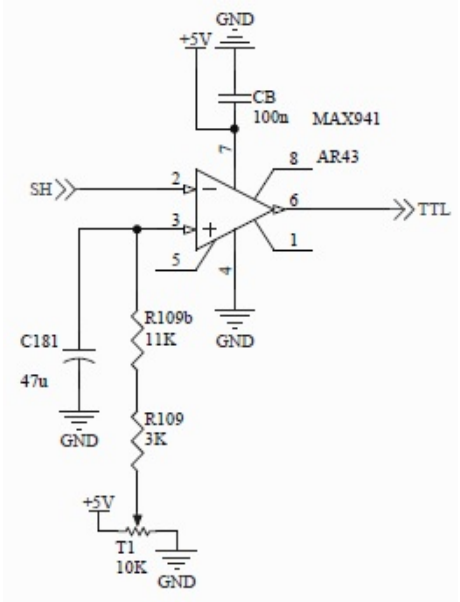

Fig. 5.5: Schematic of Single Channel Analyser configuration.

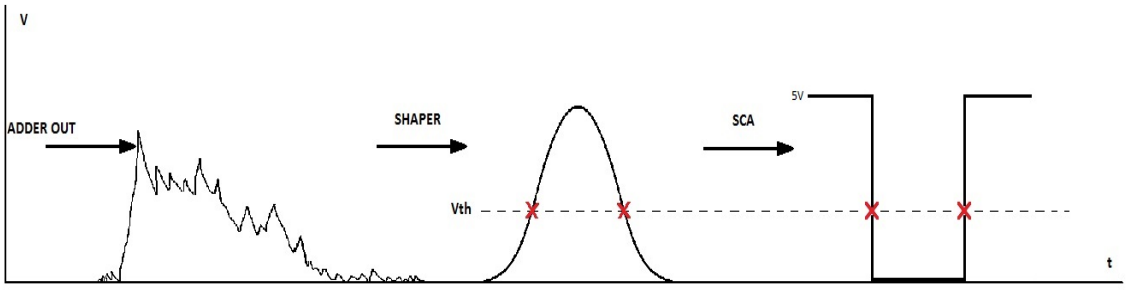

Fig. 5.6: Shaping stage and SCA for the pulse coming from the outer detector.

Now, as far as the inner signal coming from the *adder in*, it is required to be shaped for reasons similar to those concerning the outer pulse. If it were sent to the MCA with its original shape, we would have various peaks which would be recorded by the MCA as different events even if they are associated to the same one. This fact would cause an important increase in the noise and a deterioration of the energy resolution of the PE peaks. Exactly the same configuration as that we mentioned in the previous paragraph has been implemented, with an RC-CR circuit combined with an AD8051 op amp and a REF5025 voltage reference.

As the outer signal is modified by passing through the SCA, a small but measurable delay is introduced with respect to the coincident inner pulse. In order to guarantee the electronic coincidence of events occurring simoultaneously in the scintillators, we had to introduce a delay line in the inner channel. For the first layout design, we decided to provide the signal processing board with two possible delay lines: one with passive elements which could operate after the shaping stage and one with active elements and rapid response which can operate before it. As we did not know a priori the needed delay, we based our design on the previous studies at CMRP where a delay of approximately $2\mu s$ was required after the shaper, using NIM modules.

The passive delay line was made up of capacitors and inductors connected as shown in Fig.5.7. The two most important parameters we had to fix were the bandwith of the line, which had to be grater than that of the inner shaped pulse in order to not distort it, and the time constant LC, which determines the final total delay. Basing our design on the following three formulas [33], we provided the board of a 13 cells passive delay line reaching a maximum delay of 2μs:

$$\tau = n\sqrt{LC}$$

$$\sqrt{LC} = \frac{1}{\pi * f_c}$$

$$f_c \geq 2f_{max}$$

Where n is the number of cells, τ is the total delay time, f_c is the cutoff frequency (around 100kHz after the shaper) and f_{max} the maximum frequency of the signal.

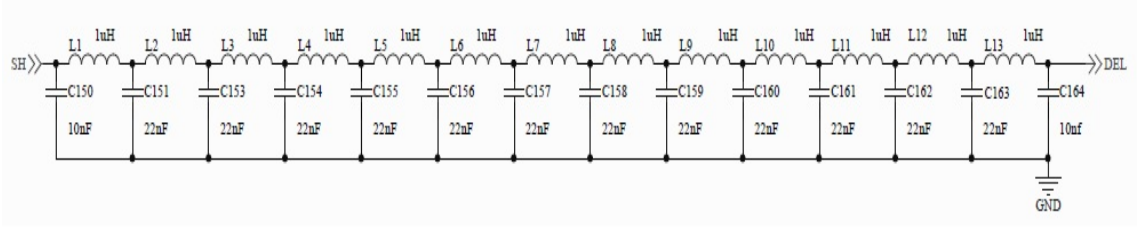

Fig. 5.7: Schematic of the passive delay line.

These previous considerations make clear why it is more convenient to use this delay line after the shaping stage: to delay a very large bandwidth signal such as that we have before the shaper, we would need much more, even hundreds, LC-cells to reach the same delay and this would be in contrast with the requirement of compactness.

The active delay line does not pose problems in terms of signal bandwith and the only parameter we are interested in is the time constant τ_{RC}. Placed before the shaper, this delay line can provide a smaller delay to the signal, thanks to the smaller width of the pulse in time scale, and with its seven stages it can reach a delay time of 1.4μs (Fig.5.8)[33]:

$$\tau = n\tau_{RC}$$

$$f_c \ll \frac{1}{RC}$$

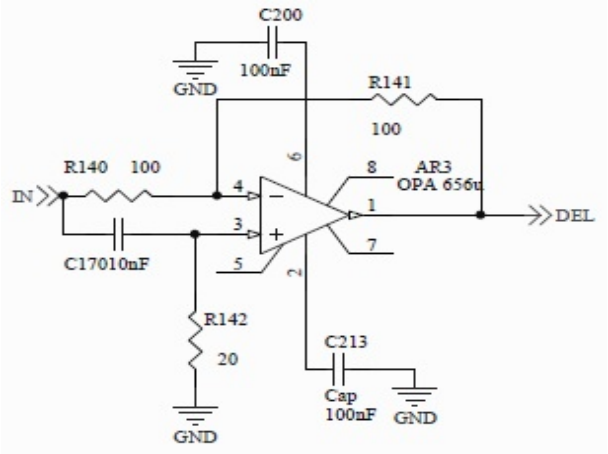

Fig. 5.8: Schematic of one stage of the active delay line (x7).

Where n represents the number of stages and f_c is rouhgly 5MHz before the shaper.

Due to the uncertainty of our expectations, we provided the board not only with a configuration allowing to choose one of these delay lines, but also with a jumper system allowing us to use an external NIM module just in case these two delay lines were not sufficient.

After these stages, both the inner and the outer signals arrive to the logic gate. If the outer logic signal is in the lower-voltage state, the coincident inner pulse is vetoed and it is not sent to the MCA. For this timing analysis, it is evident that it is very important to ensure coincidence, so that the delay lines in the processing channel of the inner pulse allow us to center the coincident pulse in the temporal window opened by the logic signal (Fig.5.9).

The Multi Channel Analyser we used for this project is a pocket MCA8000A provided by Amptek, with a conversion time smaller than $5\mu s$ ($\geq 200kcps$), a power consumption lower than 300mW with battery or DC power and with a USB-to-RS232 adapter interface.

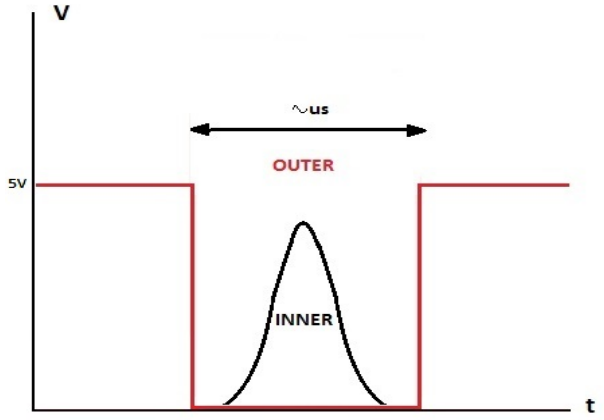

Fig. 5.9: Coincidence at gate stage in Compton suppression system.

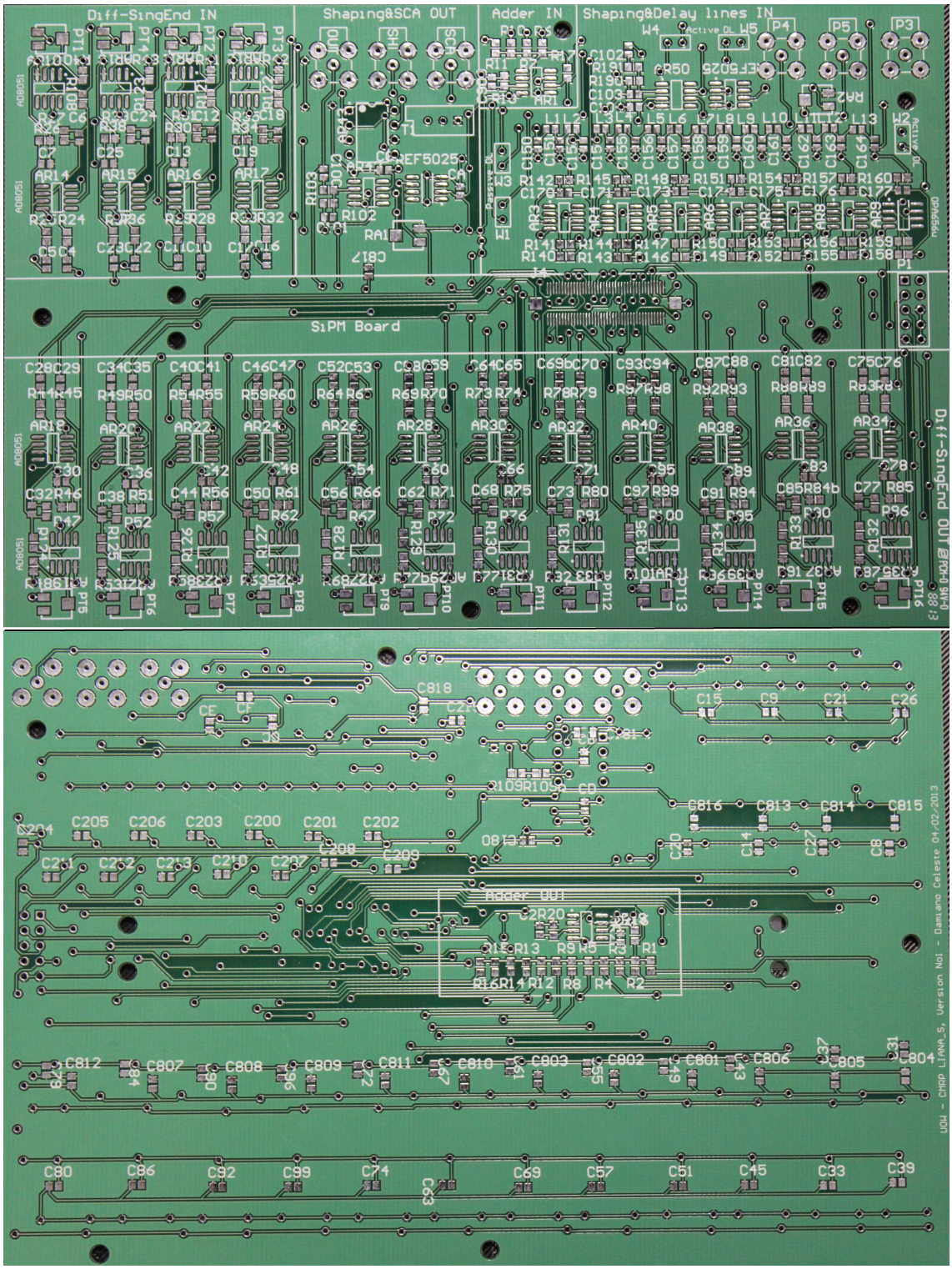

Fig. 5.10: View of the double layer signals processing board with all different stages: 80-way connector, adder IN&OUT, shaping stages, SCA, delay lines.

5.2 Power supply board

After having refined the first board, we approched the design of the board which had to lodge the power supply system.

Analysing the previous schematics and the datasheets provided by SensL concerning the SiPM and the preamplifier board, we checked all power and current requirements for the SiPM pixels and the operational amplifiers in both the preamplifier and the signal processing boards. We needed to provide the following voltages:

- Between +34V and +40V for the positive bias input.
- $\pm 5V$ for the operational amplifiers and the voltage reference devices on the signals processing board.
- $\pm 3,3V$ for the operational amplifiers on the preamplifier board.

In order to obtain these different values, we decided to provide our board with a 12V battery and to use various devices able to convert this tension into those we cited above (Fig.5.11).

The MURATA NDTD1203C and the MURATA NMK1205SC are both DC/DC converters with a 12V input voltage and dual outputs respectively of $\pm 3,3V$ and $\pm 5V$. Their output voltages are used to supply the preamplifier op amps and all other op amps in the signals processing board. Actually, as the positive voltage +5V was already provided by the regulator LM7805, we just use the negative output provided by the NMK1205SC. This regulator is essential to control and supply the last component we mention here that is the DC/HVDC converter EMCO Q01-5CRS (0-5V Input, 0-100V Output). The function of this component is to provide a voltage around 36V to the Preamplifier Board for SiPM V_{bias}. Because of this and since it is the most expensive part in our system, we have to pay particular attention to this component. This is the reason why we decided to add to this board also an electronic network allowing us to regulate the control voltage for the Q01-5CRS, before connecting it. The regulation of the input voltage is made possible through the trimmer connected to the positive input voltage +5V and the dual operational amplifier ICL7621.

Obviously, in order to connect the power supply board with the first one we described above, we also equipped both the boards with a 10-way header connector.

We finally added to this board a part with non-connected pads in order to correct possible errors in the layout design once the board was produced. We realised two boards with exactly the same size, so that we could easily assemble them through the holes which had been expressly designed.

All these parts are shown on the board in Fig.5.12 and all project files are shown in the *Appendix*.

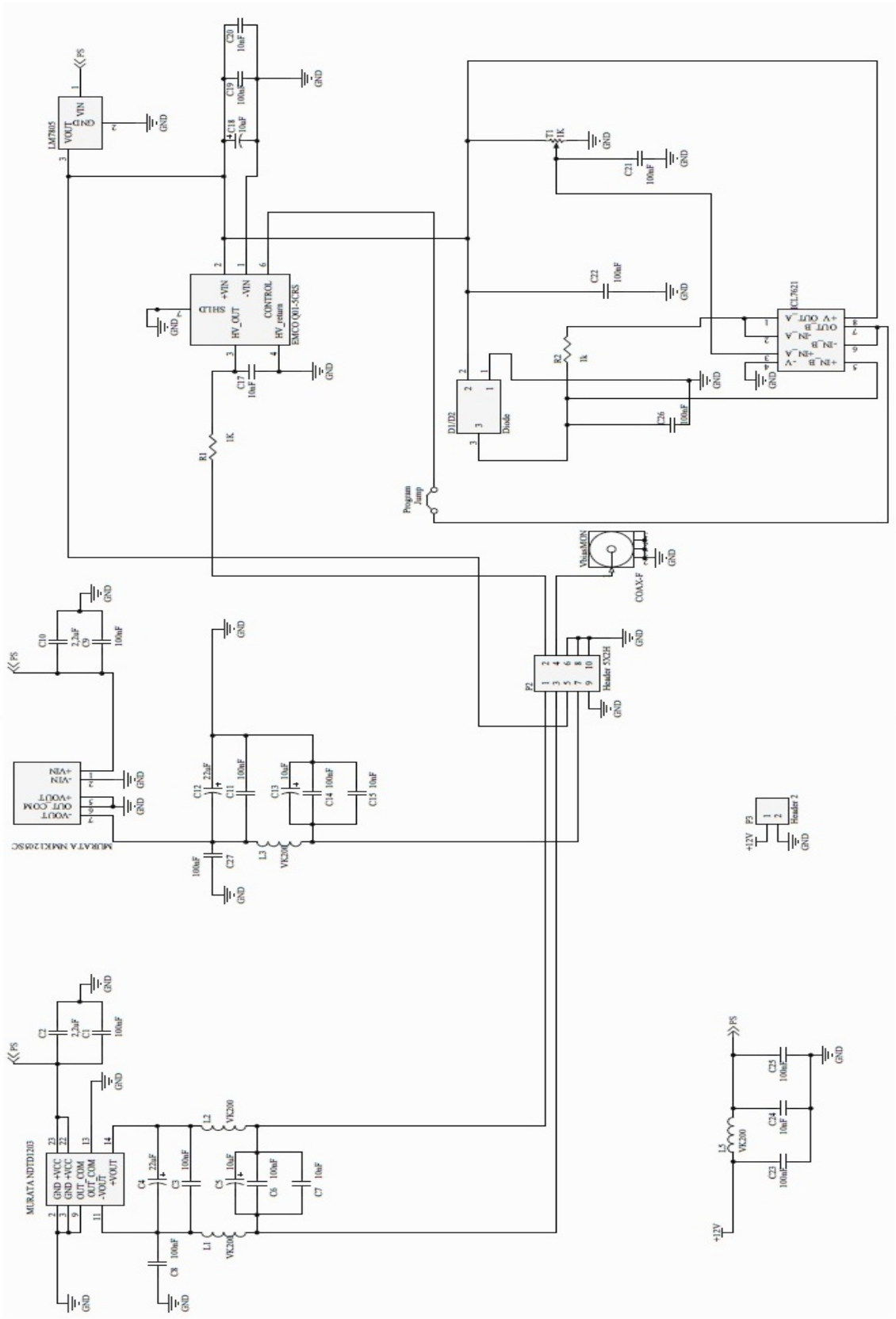

Fig. 5.11: Schematic of the power supply board.

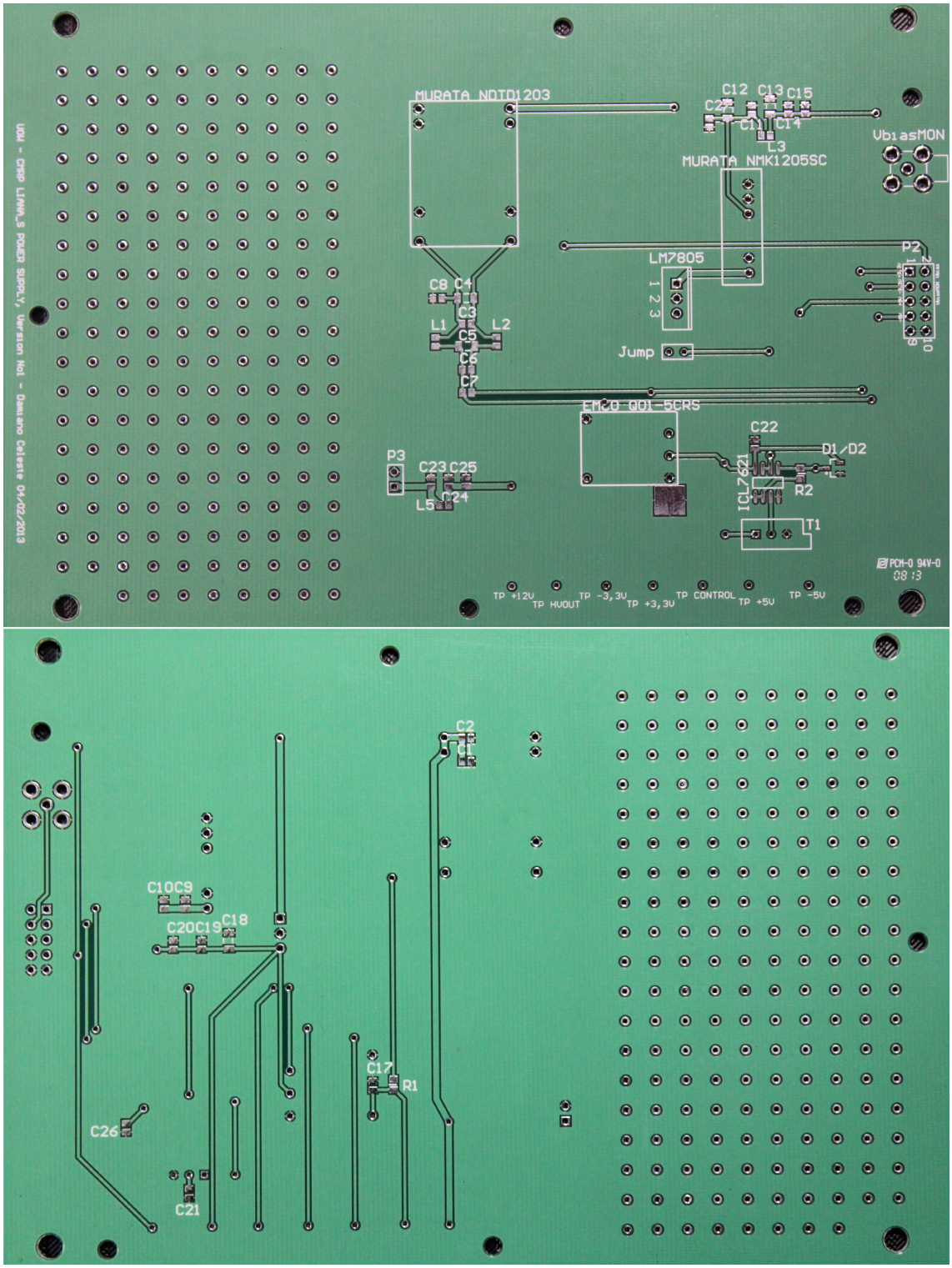

Fig. 5.12: View of the power supply board.

Chapter 6

Debugging and first results

6.1 Electronic circuit debug

Once the electronic boards were delivered, we checked that all footprints and rooting had been correctly designed and we analysed signals coming from the detectors.

First of all we soldered all by-pass parts on the Power Supply board just to check whether the 12V and the 5V were correctly provided by the external power supply and the LM7805. We consequently tested whether the control voltage system for the EMCO Q01-5CRS was working in the correct way, providing an adjustable voltage between 0 and 5V. Finally, we connected the more expensive and fragile components, the Murata DC-DC converters and the EMCO DC-HVDC converter.

The Power Supply board gave us the expected results: thanks to the NDTD1203 we had the ±3.3V needed to feed the pre-amplification board, through the LM7805 and NMK1205 we obtained the ±5V needed to feed many of the components on the Signal Processing board and, finally, the EMCO Q01-5CRS, if correctly set, provided the pre-amplification board with a 35V voltage. A voltage converter system placed on this board was able to convert the 35V into a fixed V_{bias} around 29.4V needed to let the APDs work just above the breakdown voltage at room temperature.

Before soldering all components on the Signal Processing board, we decided to test two of the DSE channels in order to verify the proper operation of both the inner and the outer signal processing lines.

Thus we checked the correctness of a DSE channel associated to one of the inner SiPM pixels and afterwards we tested the shaping stage and the delay lines. For these measurements, we placed a CsI(Tl) cylindrical scintillator (r=6mm;h=12mm) on the SiPM pixel referred to the DSE channel which was previously soldered and a ^{22}Na source close to it. This experimental setup, shown in Fig.6.1, was placed in an hermetically closed box in order to avoid any parasite current caused by external light.

As you can see in Fig.6.2, the single-ended pulse coming from the DSE circuit and its corresponding shaped pulse, after having adjusted all offsets in order to avoid overshoots, showed us that the designed circuit operated as expected. On the other side, with regard to the study of the active and the passive delay lines, a significant issue arose: whereas the active one gave us reasonable results introducing a delay time around 1.4μs according to our previous calculations, the passive delay

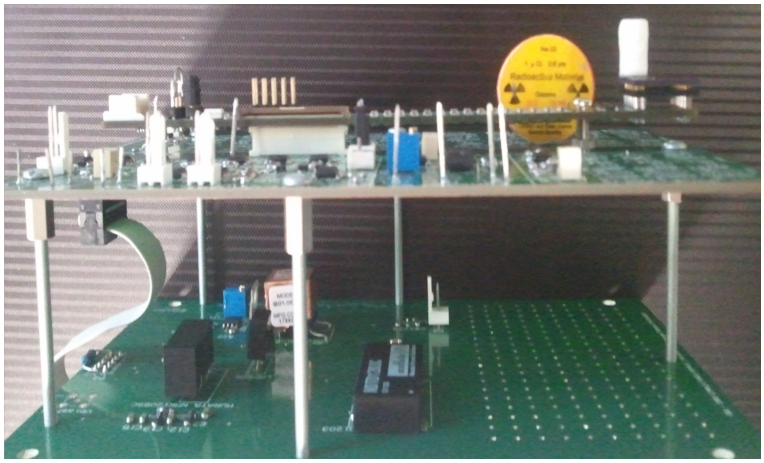

Fig. 6.1: Experimental setup of the device with the power supply board (bottom), the signal processing board (middle) and the preamplifier board (top) where the SiPM and the scintillator are located.

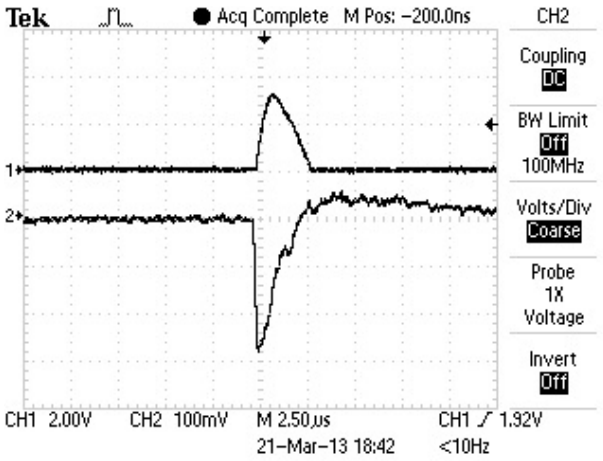

Fig. 6.2: Acquisition of the inner signal before (bottom) and after (top) shaping.

line introduced a significant signal distortion due to internal reflections. This is clearly shown in Fig.6.3 where the shaped and delayed pulses are presented and consequently we decided to exploit the active delay line for following studies and analysis.

Concerning the outer signal processing line, first of all we ensured that the DSE channel was correct, obtaining the same results as those presented above, and then we tested the shaping and the SCA stages. In Fig.6.4 the shaped pulse coming from one of the SiPM border pixels is presented as well as the corresponding logic signal generated by the comparator.

A significant mistake in the electronic design, due to inaccurate information on the SiPM datasheet provided by SensL, prevented us from starting spectroscopy. Because of a wrong numbering of the SiPM pixels, two inner channels were swapped with two outer ones, so that the geometry of our system had been altered.

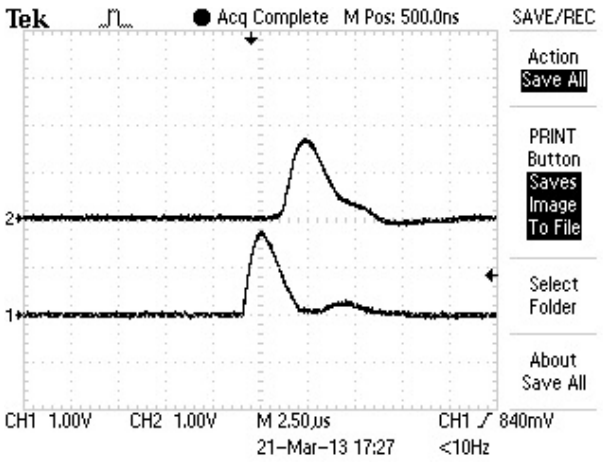

Fig. 6.3: Acquisition of the shaped (bottom) and delayed (top) signal using the passive delay line. Signal distortion clearly visible in both pulses.

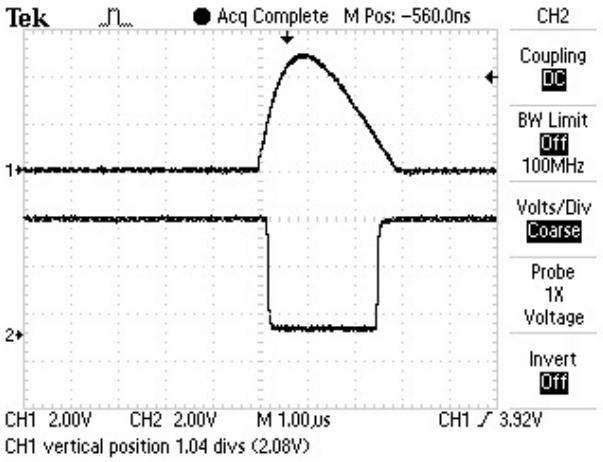

Fig. 6.4: Acquisition of the shaped pulse coming from the outer pixel (top) and the corresponding logic signal needed to veto coincident events (bottom).

Before designing and ordering a new and corrected version of the electronic boards, we decided to continue our preliminary study to check whether other parts could be modified. For this reason we prepared an experimental setup in order to test the timing characteristics of our circuit.

6.2 Coincidence analysis

We were particularly interested in testing the effective time coincidence of signals generated by simultaneous events in two scintillator crystals. In order to reach this goal, using only two of the sixteen channels (the first of them associated to one of the inner pixels and the other to one of the outer pixels), we were supposed to design an experimental setup able to generate and detect simultaneous events. We decided to use a ^{22}Na source, a β^+ unstable radioisotope, which also implies the emission of two 0,511MeV gamma-rays for each emitted positron, due to electron-positron annihilation. The momentum conservation principle imposes that these two photons are emitted in opposite directions with an angle of 180°(actually approximately 180°). Then, we put the radioactive source between two CsI(Tl) scintillators placed on the two SiPM pixels we were considering. An optical grease was used to optimise the optical matching between the crystals and the SiPM (Fig.6.5).

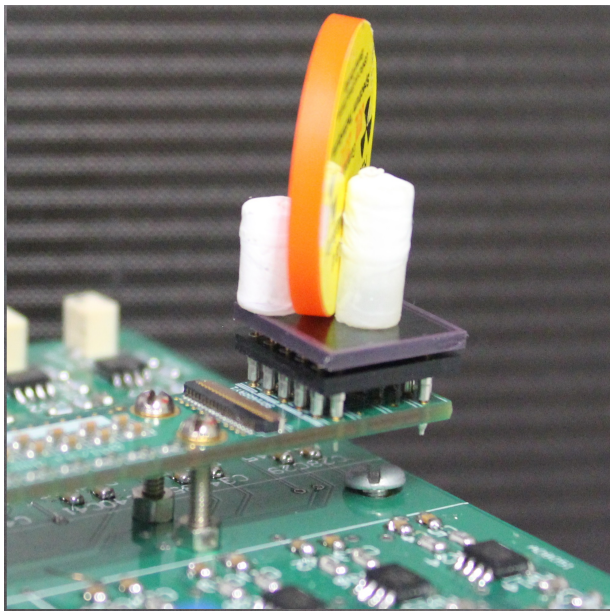

Fig. 6.5: Experimental set up for coincidence analysis.

With a 4-channels oscilloscope (Tektronix MSO4104), using its logic trigger mode, we were able to trigger coincident signals coming from the two connected pixels. First of all we ensured that the two shaped pulses were coincident, without using any delay line which could distort results. Then, after connecting the passive delay line, we immediately noticed that the introduced delay time was much greater than that we actually needed (Fig.6.6). The difference between what we expected to get (designed delay line for about 2μs) and obtained results was due to the fact that

in previous analysis at CMRP, on which we based our project, NIM modules were used: the needed delay in that case was greater because cables and other connections were used while they are not present in our system.

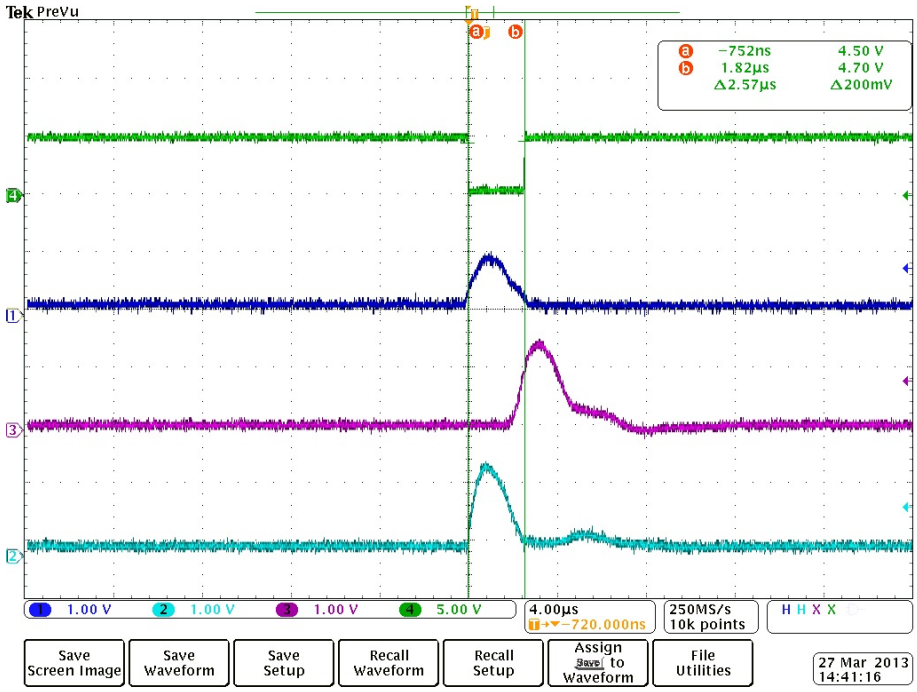

Fig. 6.6: 1)Outer shaped pulse; 2)Inner shaped pulse; 3)Delayed inner pulse; 4)Gated outer pulse.

Hence, we compared more accurately the shaped inner pulse with the logic signal generated by the SCA on the outer channel line, disconnecting all delay lines. In Fig.6.7 it is clearly shown that we had two main issues, marked with two red circles, which needed different solutions:

- As it was expected, the inner pulse was not completely vetoed by the gated pulse, so that it needed a delay time of an order of magnitude around 10^{-7}s (lower than that we supposed during the system design).
- Moreover, the gated pulse was not able to veto the final part of the inner shaped pulse. This problem would get worse with the introduction of a delay line, so that we needed a pulse stretching stage able to increase the width of the gated pulse

Both these issues had to be properly solved because they could make the anti-Compton system inefficient at low energies. Concerning the first point, we decided to use only two of the seven stages of the active delay line (Fig.6.8), providing a delay time of 200ns to the inner pulse, so that the first issue was solved at the expense of the second one (Fig.6.9).

In order to solve the second issue we needed to modify the electronic schematics and layout, modifying the SCA output.

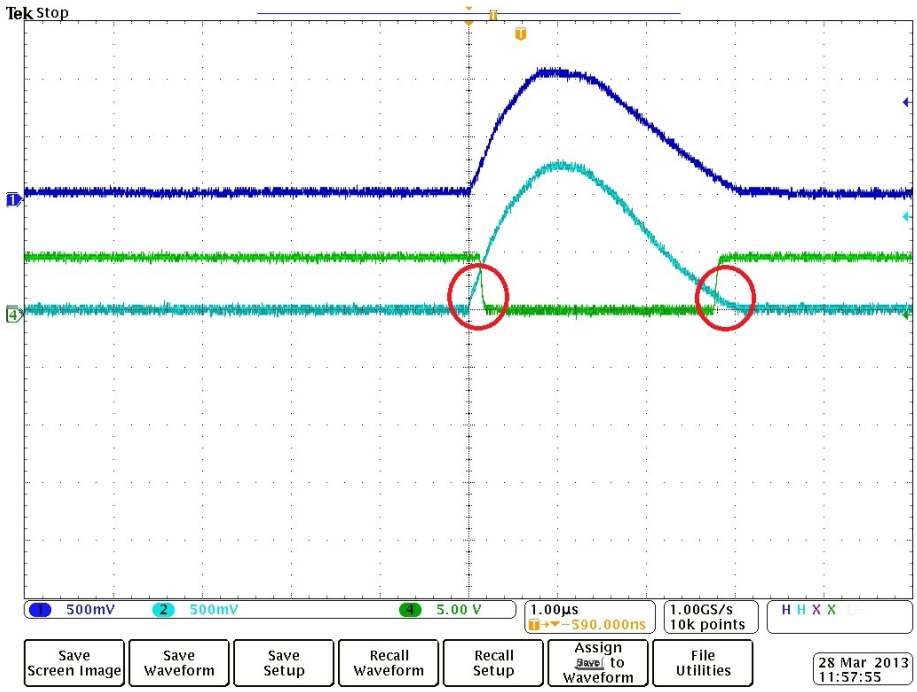

Fig. 6.7: 1)Outer shaped pulse; 2)Inner shaped pulse; 4)Gated outer pulse.

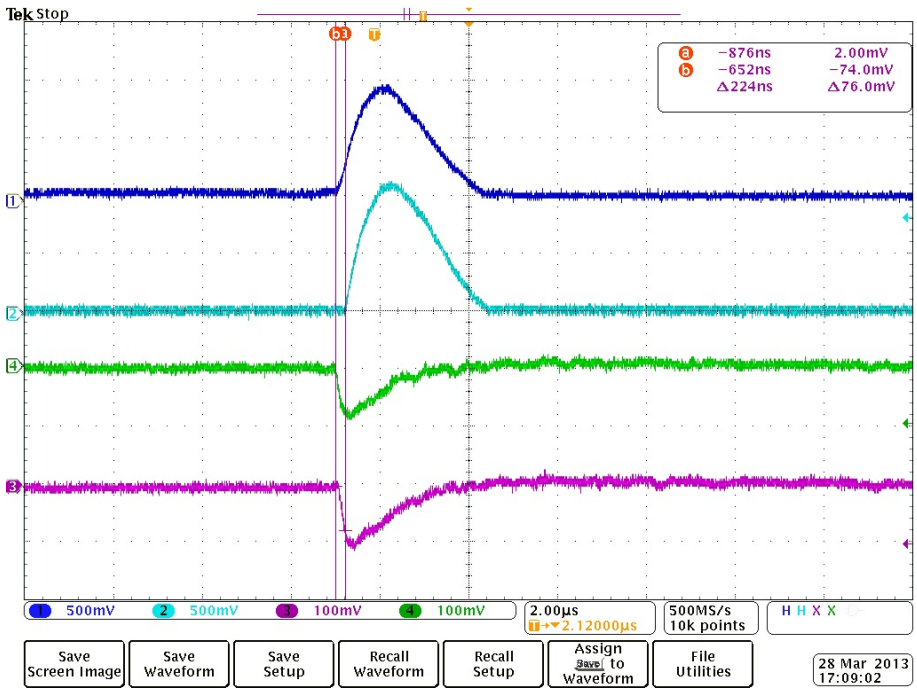

Fig. 6.8: 1)Outer shaped pulse; 2)Inner shaped pulse; 3)Inner single-ended pulse; 4)Outer single-ended pulse. As you can see, the measured delay time is 224ns.

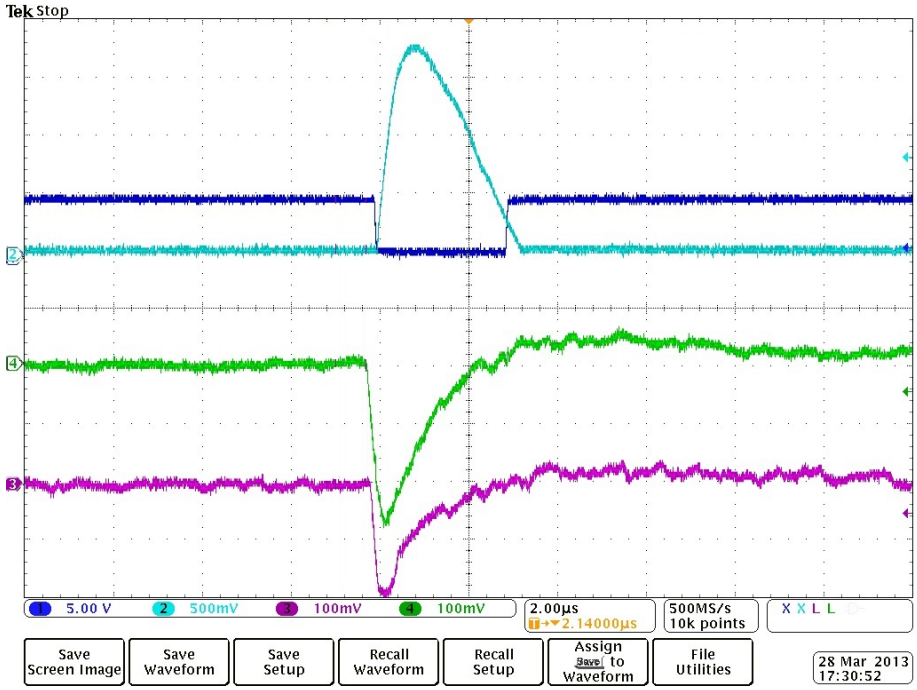

Fig. 6.9: 1)Outer gated pulse; 2)Inner shaped pulse; 3)Inner single-ended pulse; 4)Outer single-ended pulse.

The pulse stretcher and all other changes in the electronics layout are presented in the next chapter.

Chapter 7

New layout

As we mentioned in the last chapter, according to our measurements it was required to provide our Signal Processing board with a pulse stretching stage able to increase the logic pulses width.

For this reason, we decided to use a LM555 Timer by Texas Instruments in monostable operation, wired as a one-shot with a resistor and a capacitor which are supposed to introduce the needed delay. The operation of this circuit is clearly explained in Fig.7.1 which is related to the schematic reported right below in Fig.7.2:

1. The capacitor is initially grounded when the input trigger is HIGH, so that the output is LOW.

2. When the input trigger drops to the LOW state and it is below $\frac{1}{3}V_{CC}$, the capacitor C starts charging through the resistor R and the output is driven HIGH.

3. When V_C reaches $\frac{2}{3}V_{CC}$, the LM55 discharges the capacitor to ground and its output returns to LOW. The output pulse width is equal to τ=1.1*RC.

We must remark that LM555 triggers input signals on the falling edge, so it is intrinsically an inverting device: this fact did not represent an issue in our case because we had a MCA with two gates which can work with opposite logic signals.

Beside this important modification of the electronics, some other changes were required in order to optimise our system and to do spectroscopy:

- Inverting two inner channels to associate them to the right SiPM pixels, as we mentioned in the previous chapter.

- Inverting differential input signals, in order to obtain positive input pulses for the MCA.

- Changing the EMCO DC-HVDC device providing the V_{bias} to the SiPM pixels.

This last change was required because the EMCO Q-series device needed a load resistor to be controlled and to set the right output voltage, increasing temperature and V_{bias} instability. Without using a load resistor this device gave us a bistable

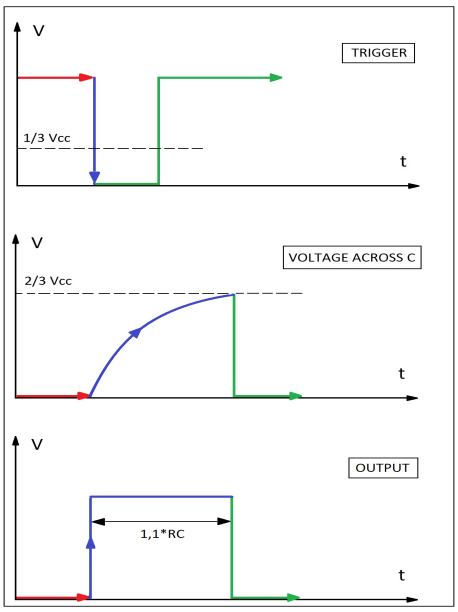

Fig. 7.1: Sketch of the monostable operation: the input trigger coming from the comparator (top), the voltage across the capacitor C (middle) and the LM555 output signal supposed to veto coincident pulses at the following gate stage.

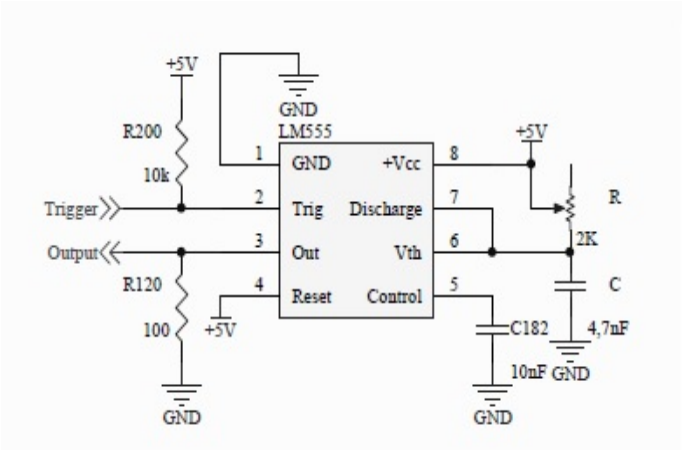

Fig. 7.2: Schematic of the pulse stretching stage between the comparator and the MCA.

output of 0V or 100V and we could not gradually change the output voltage, as shown in Fig.7.3.

Consequently we decided to use the EMCO CA02P-5 which allowed us to gradually set the output voltage without using any load resistor. The schematic of the new DC-HVDC converter is presented in Fig.7.4 and the second version of our boards is presented in Fig.7.5. All project files concerning these parts are reported in the Appendix.

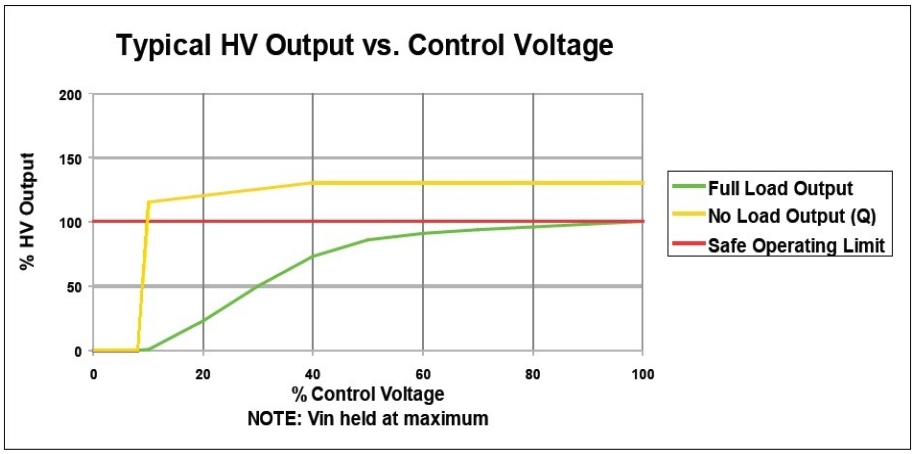

Fig. 7.3: Behavior of the Q01-5CRS proportional DC-HVDC converter with or without load.

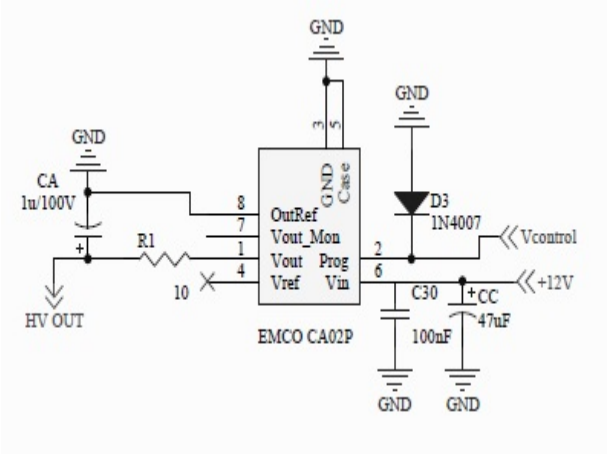

Fig. 7.4: Schematic of the CA02P regulated DC-HVDC converter supposed to provide a voltage between 30V and 40V in order to bias the SiPM pixels.

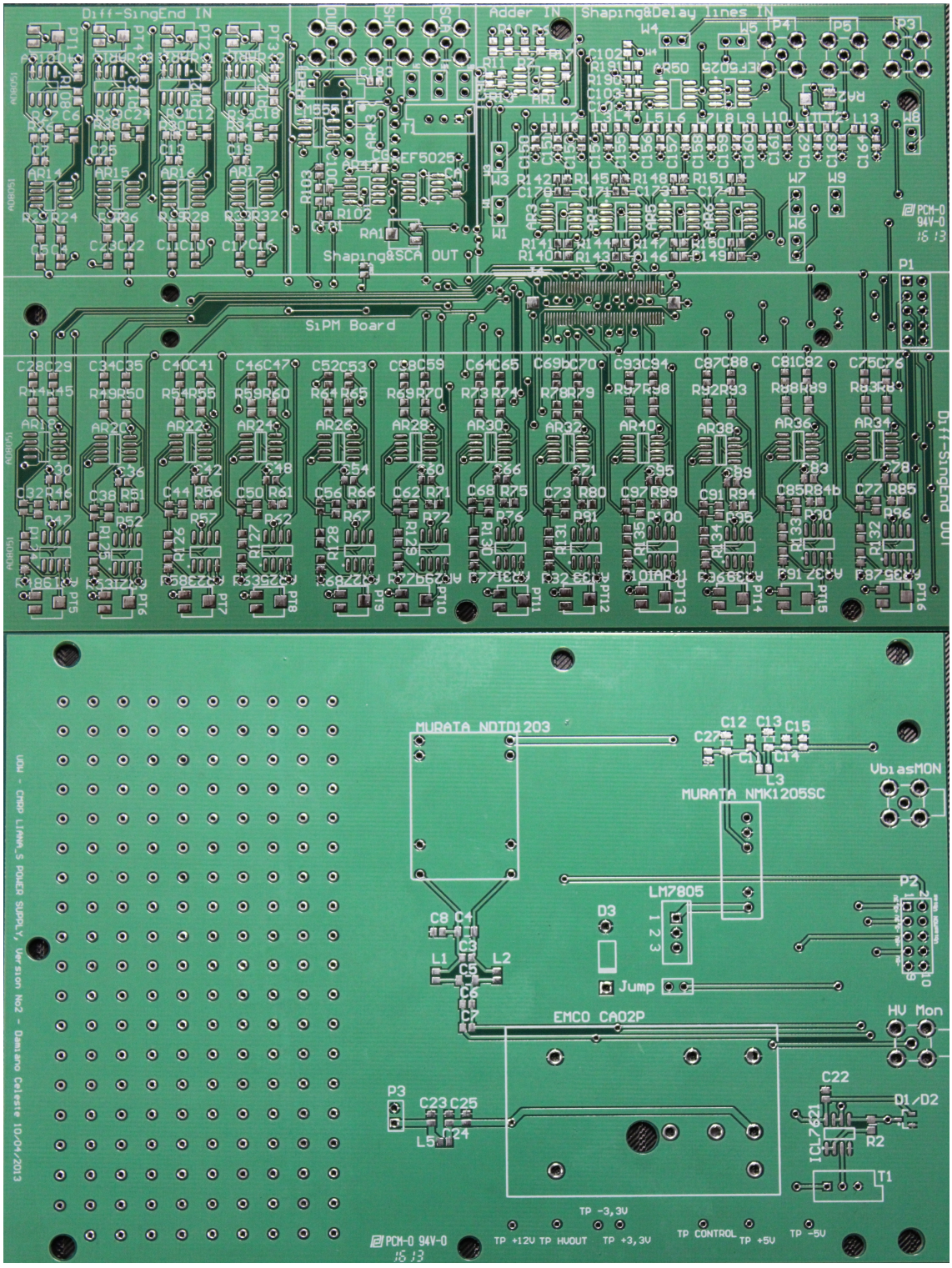

Fig. 7.5: Second version of the electronic boards: Signal Processing board (top) and Power Supply board (bottom).

Chapter 8

Results

The second version of the electronics was tested to verify that all parts were correctly designed and that signals coming from the SiPM were correctly processed.

First of all, we checked whether all components, which were changed or added to both the boards in comparison with the first version, operated as expected. Thanks to the new DCHV EMCO converter we were able to gradually regulate the V_{bias} finding the optimal gain for the SiPM and thanks to the LM555 we could adjust the time width of the gated outer pulse.

Afterwards we were supposed to optimise all electronic parameters in order to obtain proper signals to do spectroscopy and anticoincidence, and in particular:

- The V_{bias} affecting operation of SiPM pixels and their gain.
- The shaping time and gain for both the inner and the outer channels.
- The time width of the digitised outer pulses.
- The delay time in the inner channel to ensure signal coincidence.
- The noise baseline in order to increase the signal to noise ratio.

After the preliminary SiPM characterisation presented in the 4th chapter, we knew that the breakdown voltage for this detector was approximately 27V and that the V_{bias} would be fixed roughly 2V above the V_{BD}. Starting from 29.7V and gradually decreasing the V_{bias} with steps of 0.1V, we tried to find the optimal gain for the SiPM pixels in order to avoid signal saturation ($\leq 5V$) in both the inner, where four pixels were added, and the outer channel, where twelve pixels were added.

Obviously, this goal was also reached by modifying the inner and the outer shaping time and gain finding the optimal values of the RC-CR filter. We finally chose a shaping time $\tau_{IN} = RC + CR \approx 4\mu s$ and $\tau_{OUT} \approx 2\mu s$, where the first one was greater than the outer one in order to obtain proper signals to be sent to the MCA for amplitude analysis.

The optimisation of gain and bandwidth also aimed to partially reduce the signal to noise ratio which would affect the quality of Compton suppression.

Thanks to the pulse stretching stage on this second version, we could obtain a longer gated pulse reaching approximately 8μs, a reasonable time width to ensure anticoincidence.

As the pulse stretcher introduced an additional delay time to the outer pulse, we had to provide the inner channel with a delay line compound by four active stages with a $\tau_{RC} = 100ns$ each (400ns), differently from what we supposed before.

A screenshot from the oscilloscope of coincident signals is shown in Fig.8.1.

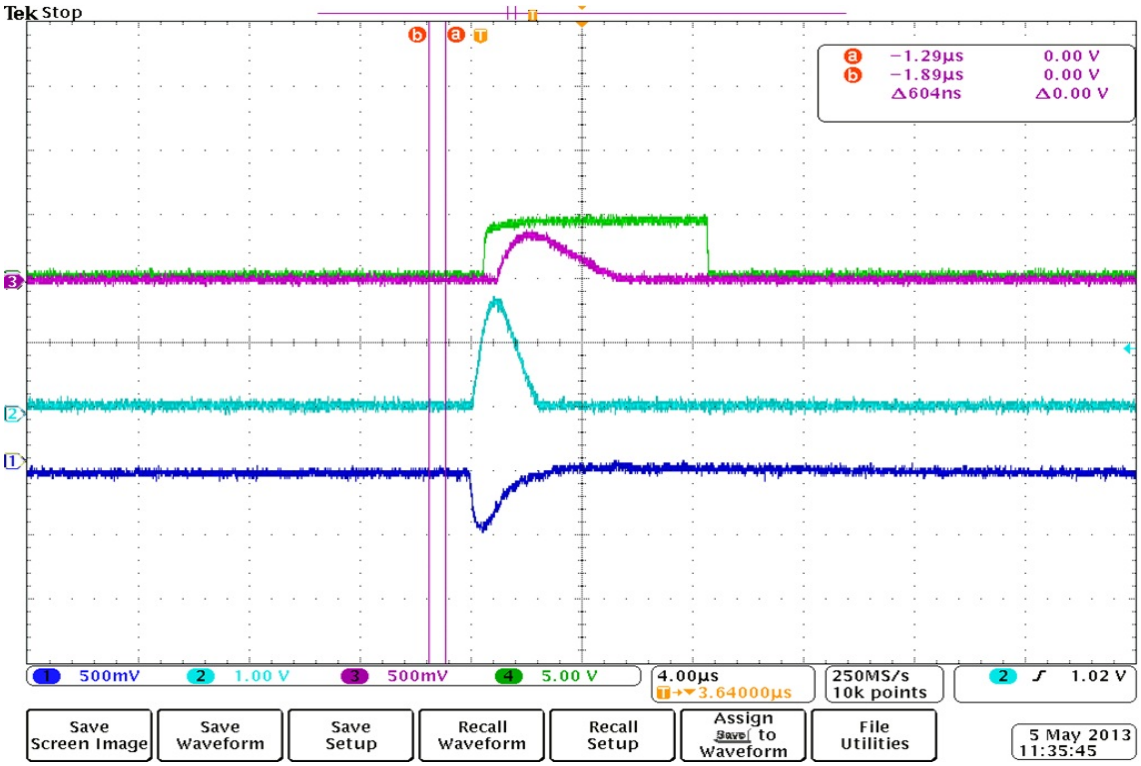

Fig. 8.1: 1) Outer signal before shaping 2) Outer shaped signal 3) Inner shaped signal 4) Outer gated signal

The system shown in Fig.8.2 was placed in a dark box, in order to reduce distortion of final results due to external light.

The Signal Processing board was placed above the Power Supply board and they were connected through a 10-way cable in order to feed all electronic components. The Preamplification board provided by SensL was connected to the first one through the 80-way board-to-board connector and the SiPM was placed on its support.

Using the same experimental set-up presented in the previous chapters, we started with the characterisation of the inner scintillators.

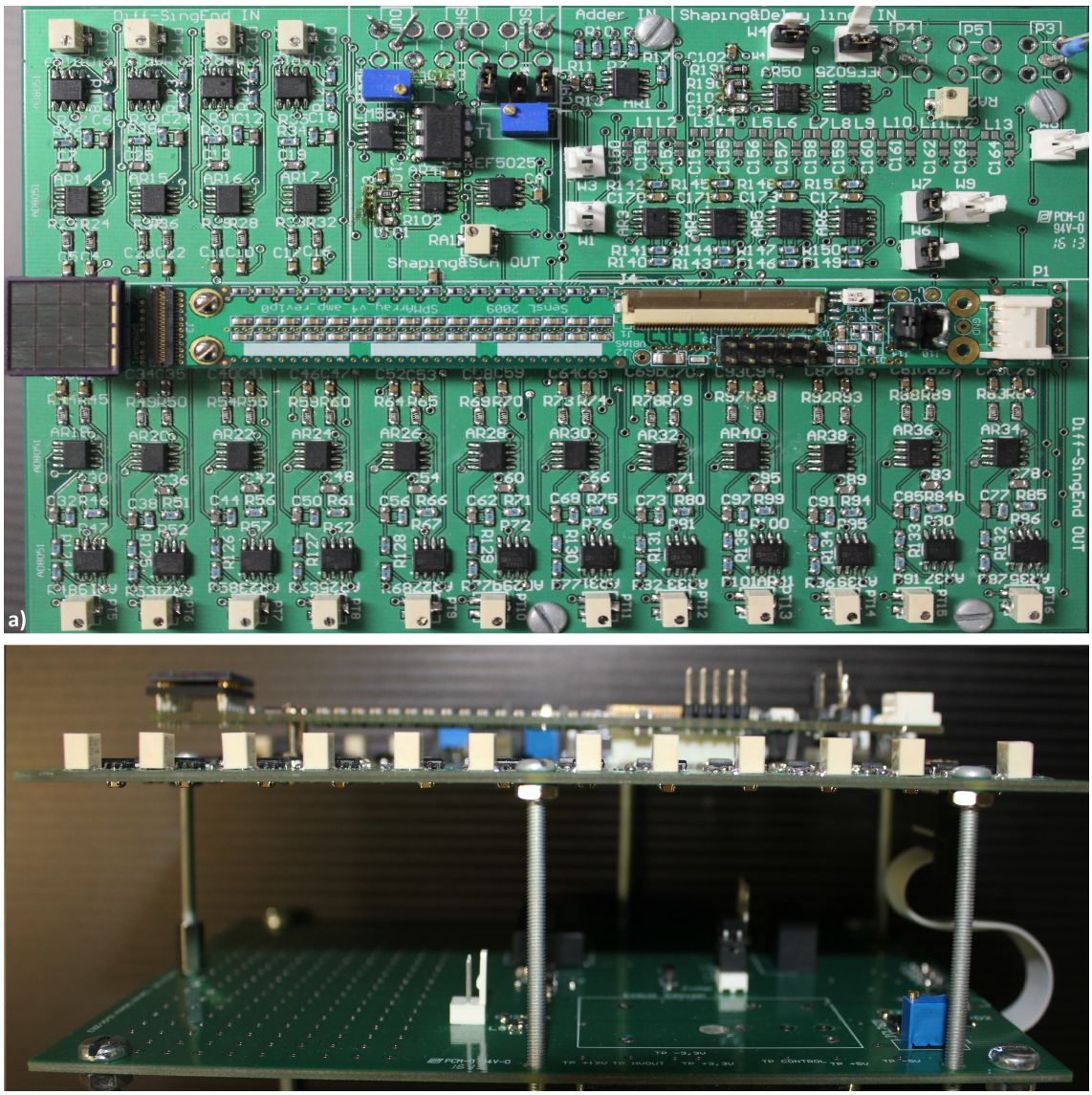

Fig. 8.2: a) Top view of the Signal Processing board and the Preamplifier board with the SiPM connected on the left side; b) Side view of the system with the Power Supply board (bottom) and the Signal processing board (top).

8.1 Characterisation of inner scintillators

Before starting with anticoincidence tests, we were interested in testing all the inner scintillators in terms of energy resolution and range using the SiPM to read out the signals coming from the crystals and using this new electronics and experimental set-up.

We tested three different crystals with a diameter of 6mm matching the four inner pixels and with different height (6,9,12mm). An optical grease was used to couple the crystals with the SiPM. For this test we acquired a ^{137}Cs spectrum for each crystal and we obtained the results shown in Fig.8.3.

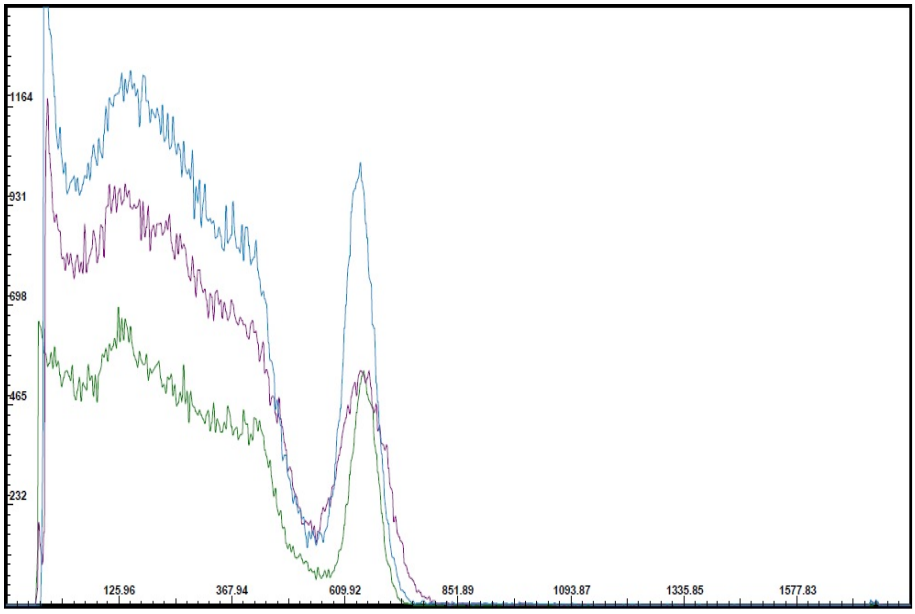

Fig. 8.3: ^{137}Cs spectrum acquired with three different inner scintillators with different height: 6mm (green), 9mm (violet) and 12mm (blue)

HEIGHT	FWHM	COUNTS
6mm	9,3%	7986
9mm	15,7%	13545
12mm	11,4%	17534

Table 8.1: Resolution and data colleted for 1000s referred to the 662keV peak.

For these three 1000s acquisitions the most important parameters are reported in Tab.8.1. These results showed a great difference between the crystals in terms of energy resolution, so that the 6mm was supposed to be the best choice for future experiments, probably due to the different conditions of their surfaces. In fact, analysing their surfaces with a microscope, the 9mm crystal showed to have a much more deteriorated surface if compared to the others, causing its bad performance.

The distance from the source was fixed and thus we could remark different count rates which increased because of the increasing sizes. Unfortunately, owing to the

great non-linearity of the MCA at lower energies, we could not quantify the energy range, even if it was clear from the spectra that the 6mm high crystal was able to ensure a larger energy range. Given these results, for our anticoincidence measurements we decided to use the 6mm inner crystal, ensuring the best performance.

8.2 Anticoincidence measurements

The last analysis aimed to test the real efficiency of our system in terms of anti-Compton spectrometry, and we focused on some preliminary issues:

- The V_{th} on the outer channel finding the optimum for Compton suppression.
- The position of the source with respect to the crystal and how this factor could affect Compton suppression.
- The optimisation of outer crystal shape and size.

Beside these points, the darkness of the box, the perfect alignment of the crystals avoiding cross-talk as well as light sharing and other important issues such as temperature stabilisation should be taken into account to optimise Compton suppression.

8.2.1 Compton suppression as a function of V_{th}

The threshold voltage designed to digitise the outer signal, which is in the low/high logic level if it is respectively below/above this threshold, can affect the efficiency of Compton suppression.

Generally speaking, the lower the threshold is the better the anti-Compton efficiency is, by maximising the suppression of the Compton continuum and leaving the full energy peaks unchanged. However, if the threshold goes too low and below the noise baseline the gated signal starts to be stable in the high logic level, vetoing non-coincident events as well. In this case, what happens is that we suppress all events regardless if they are Compton events or not and we can remark the suppression of the full energy peaks as well.

Because of this, it was crucial to find the minimum V_{th} for each configuration as it is shown Fig.8.4.

From these spectra it is clear that changing the threshold we obtain different results in terms of Compton suppression. Using different outer crystals, the baseline and so the minimum V_{th} change dependently from their surfaces quality and their shape, which affects light collection. Actually the noise baseline is very high also because twelve signals and, along with them, their associated noise are added on the outer channel. In addition, the count rate of the outer detector is orders of magnitude bigger than the inner one due to the bigger volume: this fact could cause a great number of casual coincidence and negatively affect Compton suppression.

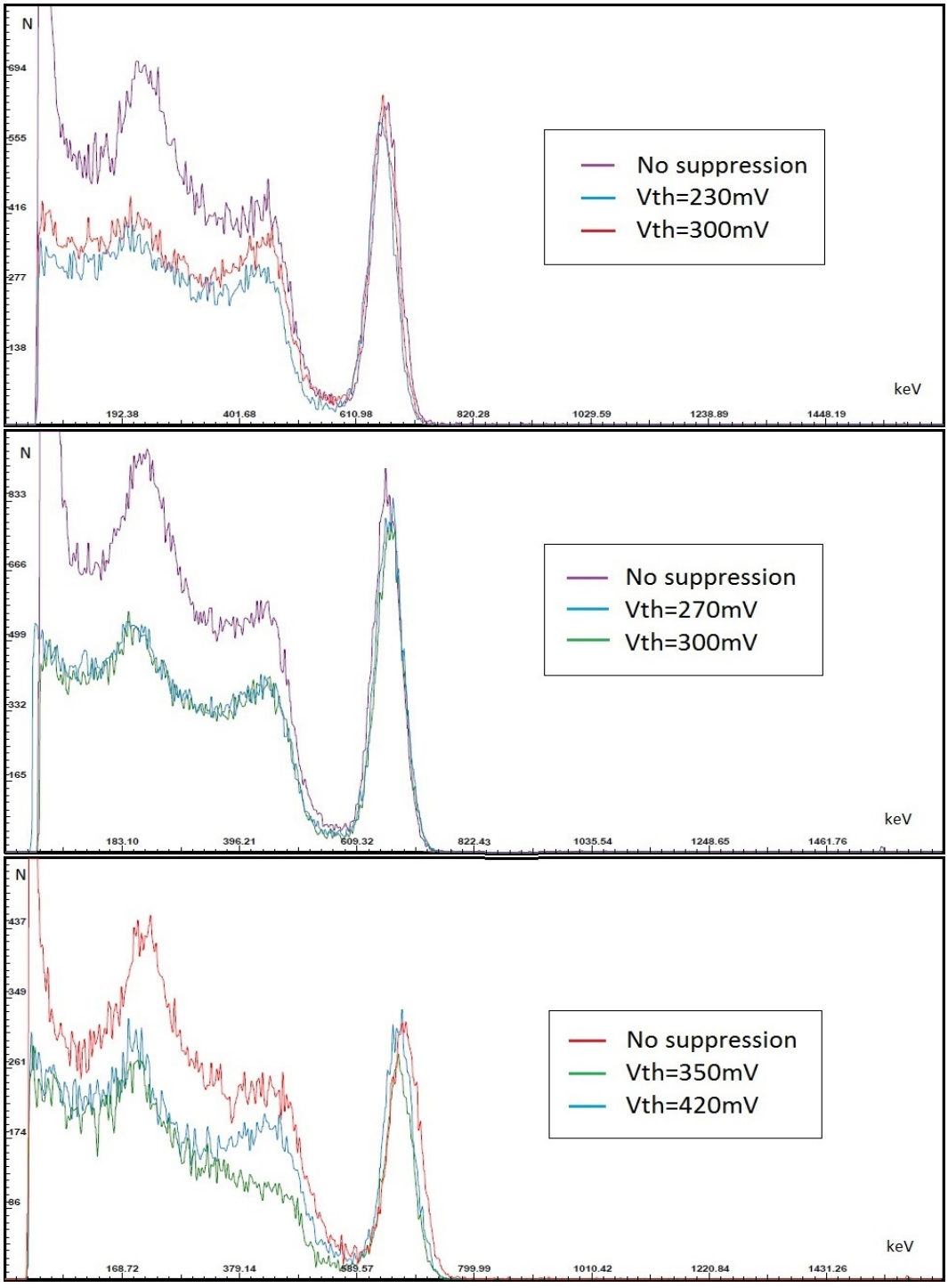

Fig. 8.4: ^{137}Cs spectrum acquired with three different outer scintillators with different shape and size, coupled with the 6mm inner scintillator: cylindrical outer crystal with a bigger angle (top), cylindrical outer crystal with a smaller angle (middle) and pyramidal outer crystal (bottom).

In Fig.8.5 the results obtained with the pyramidal outer crystal are shown, starting from a threshold close to 0mV and gradually increased reaching the situation without Compton suppression. For lower thresholds just a few events are recorded by the MCA at lower energies, due to bremsstrahlung effect of electrons in CsI(Tl). The increasing threshold gradually reveals the full energy peak until it is completely shown at 400mV.

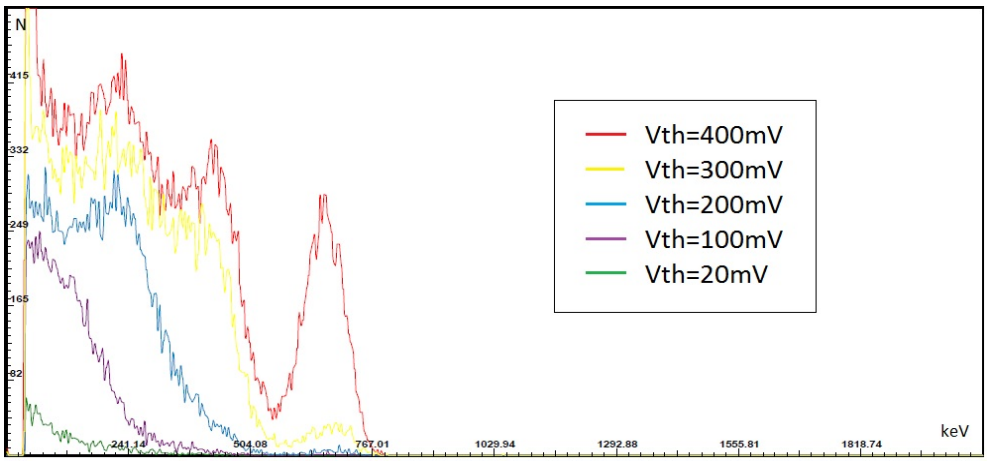

Fig. 8.5: ^{137}Cs spectrum acquired with the pyramidal outer crystal, coupled with the 12mm inner scintillator, for different thresholds.

8.2.2 Compton suppression as a function of source position

As the Compton effect is not an isotropic phenomenon, especially for those photons with energies around hundreds of keV, the position of the radioactive source with respect to the crystals was another important parameter to be taken into account in order to optimise the anti-Compton efficiency.

In the next pages we present all the results obtained using the pyramidal outer scintillator and acquiring ^{137}Cs spectra for 1000s.

In Fig.8.6, where the source was placed on the top of the system, the anti-Compton efficiency reached 15.8%, calculated taking into account the Compton continuum, through the ratio $\frac{Area_{withsuppression}}{Area_{withoutsuppression}}$. The sketch on the right side of the picture shows how the anisotropy of Compton effect can affect efficiency: considering an arbitrary point of interaction (blue point at the center of the inner crystal) and the Compton angular distribution (red ellipse around the point of interaction), it is clear that photons which are scattered in those two solid angles around 0° and 180° cannot be detected by the outer detector. The yellow areas inside the angular distribution represent the probability that scattered photons are not detected.

Given these considerations, the probability of not detecting photons releasing a small amount of energy within the inner crystal is much bigger than that of backscattered photons. This is actually evident in the reported spectra where Compton suppression is less efficient at lower energies.

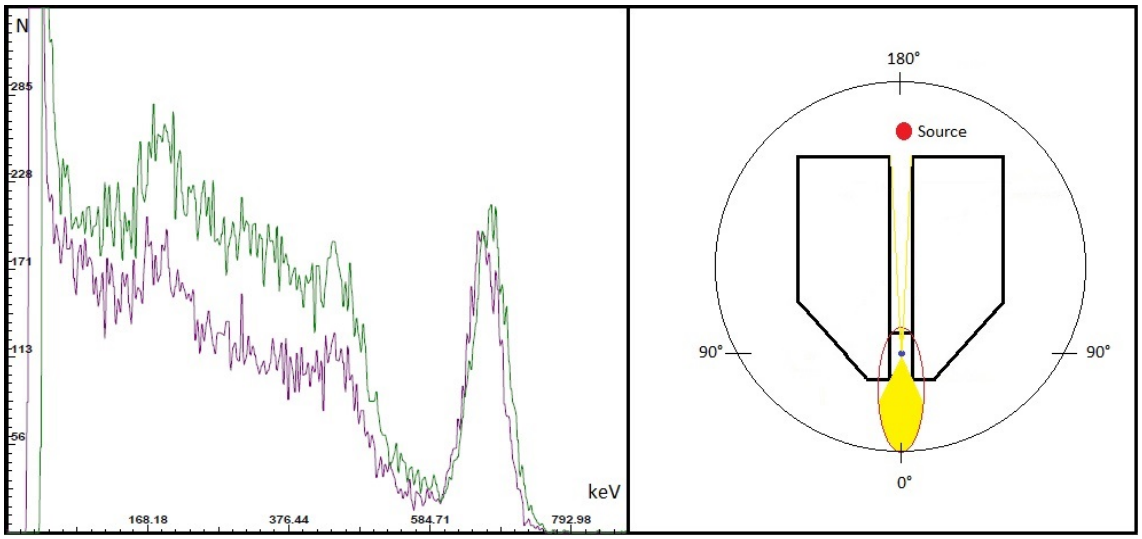

Fig. 8.6: ^{137}Cs spectra acquired with the pyramidal outer crystal, with and without compton suppression (left), and sketch of Compton angular distribution referred to this configuration with the source on the top (right).

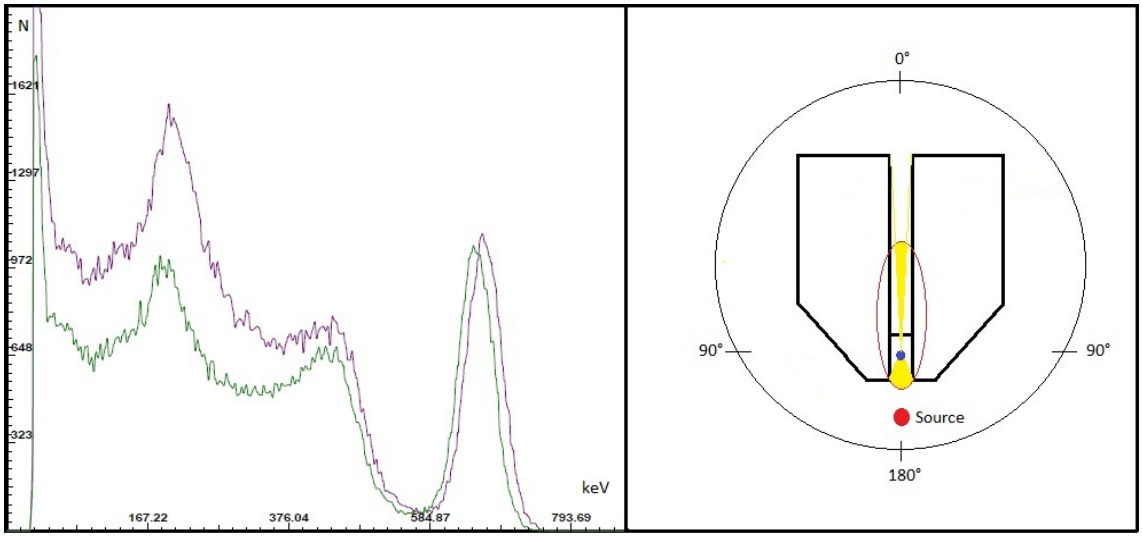

Fig. 8.7: ^{137}Cs spectra acquired with the pyramidal outer crystal, with and without compton suppression (left), and sketch of Compton angular distribution referred to this configuration with the source on the bottom (right).

For these reasons, we put the ^{137}Cs source in the opposite position, right under the crystal. In Fig.8.7 it is shown the probability of not detecting scattered photons is much smaller than the previous case and backscattered photons in this configuration are not detected by the outer crystal. In these spectra, unlike the previous ones, you can notice that Compton suppression is more efficient at lower energies and we reached a factor of 27.5%.

The best results were obtained placing the source on the side of the crystal, as shown in Fig.8.8. In this configuration we minimised the issue concerning the undetected photons because the probability of 90° scattering is the lowest possible. At the same time, we did not obtain a considerable improvement of anti-Compton efficiency (28.2%) because the outer volume able to detect forward Compton scattering was much smaller compared to the previous case.

After these measurements, we decided to place the source on the side of the crystal and to continue anti-Compton optimisation maintaining this configuration.

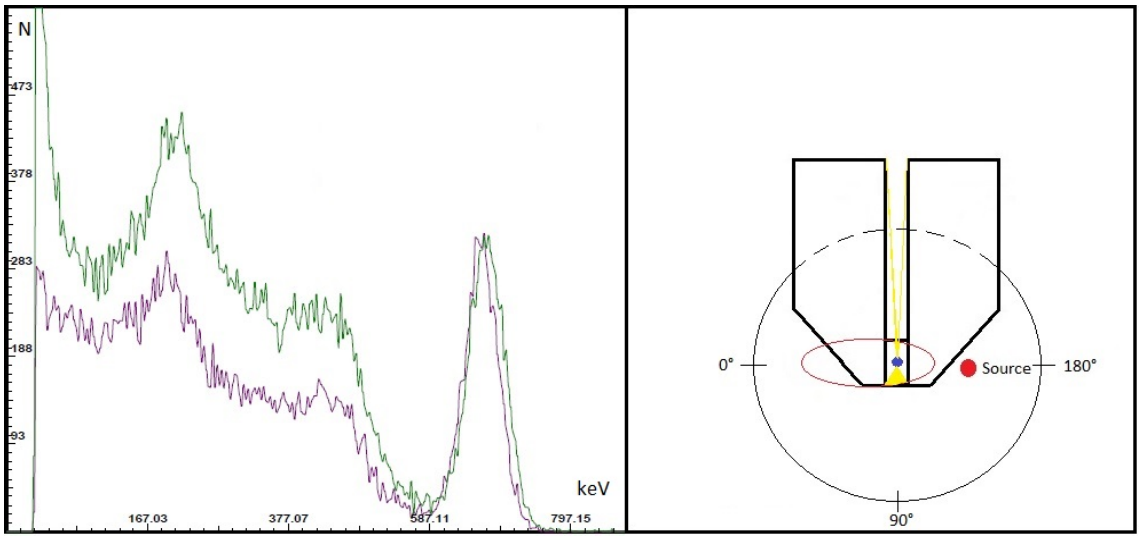

Fig. 8.8: ^{137}Cs spectra acquired with the pyramidal outer crystal, with and without compton suppression (left), and sketch of Compton angular distribution referred to this configuration with the source on the side (right).

8.2.3 Optimisation of Compton suppression

After finding the optimum using the pyramidal outer detector, we tested the other two outer detectors optimising the alignment between crystals and the SiPM.

One of the main issues for these cylindrical crystals was that they did not cover the whole area of the SiPM, whose edge pixels can be excited by external light. This fact could distort results, especially if the environment is not perfectly dark. Moreover, the smaller volume of these crystals compared to the pyramidal one makes them less adequate to detect scattered photons.

Nevertheless, the results we obtained using this outer scintillators were much better than those presented in the previous paragraph, reaching efficiencies of 39.4%

for the crystal with a smaller angle and 40.8% for the other one (Fig.8.9).

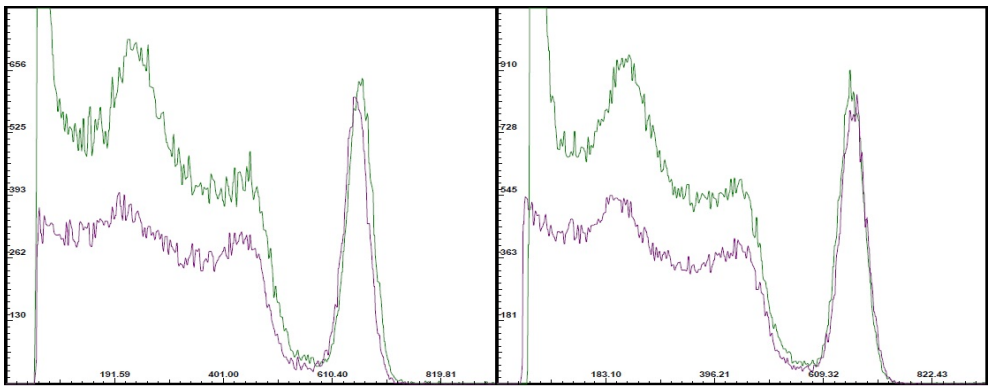

Fig. 8.9: ^{137}Cs spectra, acquired with and without compton suppression, using the cylindrical-conical crystal with a bigger angle (left) and a smaller angle (right).

We could explain this unexpected result by the quality of the crystals themselves. In fact, even if the pyramidal crystal would theoretically be the best one in terms of shape and size, it was the oldest one and its surface, which had been mechanically modified in order to avoid crosstalk between pixels, had many imperfections. On the other side, the two cylindrical-conical crystals, which were not as old as the first one, were in very good conditions in terms of surface quality and in order to avoid crosstalk an optical paint was used, as explained in the 3rd chapter.

In Fig.8.10 previous results obtained at CMRP are presented. Using the same read-out configuration and NIM modules instead of the new electronics (a), the anti-Compton efficiency reached much smaller values than those presented above. Our results are rather comparable to those obtained using a PMT to read out the outer detector (b), with a much higher PDE compared to SiPM at those wavelengths, and this fact leads us to be satisfied with this first version of the device.

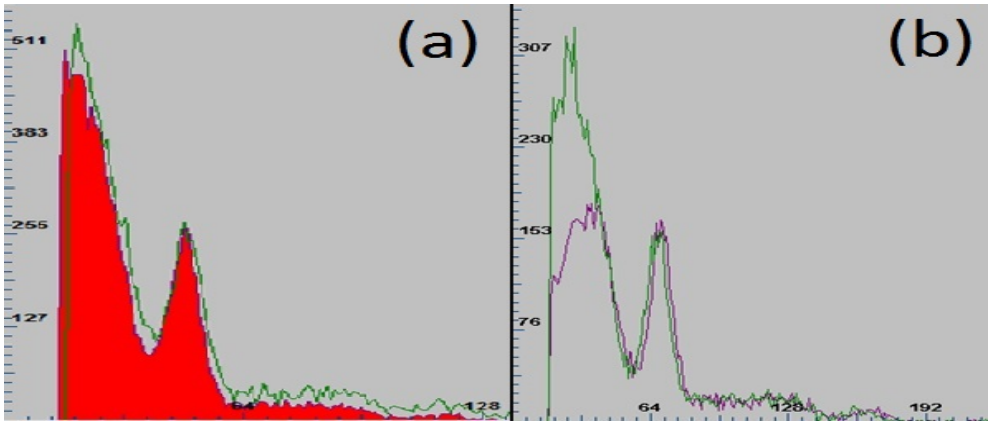

Fig. 8.10: ^{137}Cs spectra, acquired with and without compton suppression, using a SiPM to read out both the inner and the outer CsI(Tl) crystals (a) or using a PMT to read out the outer detector (b).

Chapter 9

Conlusions and perspectives

The preliminary characterisation of the two SiPMs and of all the CsI(Tl) crystals, using PMT, was successfully performed. The schematics of the electronic circuits able to read out the SiPM were realised and the layout of the electronic boards was designed, ensuring compactness and functionality.

This first version of the electronic boards was analysed to find any errors and it was used to do coincidence analysis in order to understand which parameters were wrongly designed. Once the debugging of the first version was done, a second version of the boards was designed and realised, obtaining a perfectly working system which was able to process signals coming from the SiPM to carry out spectrometry and Compton suppression.

Firstly, before starting spectroscopy measurements, we optimised all the electronic parameters. This long stage of optimisation aimed to obtain adequate signals which must have good timing and amplitude features to be recorded by the MCA (inner channel) and to allow anticoincidence (outer channel). In the final set-up, the inner signal had a time-width of $4\mu s$ and an amplitude around 2.5V (at 662keV), and the gated outer pulse had a time-width of $8\mu s$ and, obviously, an amplitude of 5V.

We could perform further characterizations of all inner crystals using the new read out configuration reaching energy resolution of 8-9% at 662keV. Finally, we started anti-Compton measurements finding the optimum in terms of threshold voltage on the outer signal, source position and outer crystal shape and size. We could check the quality of the Compton suppression system comparing efficiencies obtained with different configurations. We performed all preliminary basic studies of main parameters reaching an anti-Compton efficiency of 40.8%.

The best configuration was achieved using the cylindrical-conical crystal with a bigger angle as outer scintillator, the 6mm high crystal as inner scintillator, the threshold fixed at 300mV and the source placed on the side of the crystals.

Comparing our results with those obtained a few years ago at CMRP, we could remark that this first version of the electronics, designed for this innovative device, brought many improvements and laid foundations for future researches.

It is evident that many progress can be made by investigating and optimising other parameters.

One of the most important issue in our measurements for example was the shif-

ting of the spectra in subsequent measurements. This was due to temperature sensitivity of the SiPM which affected the operation of the pixels and their gain. For this reason, it will be required to provide the photo-detector with a temperature stabilisation system.

The electronic boards can be reduced in terms of sizes and modified in order to further minimise current absorption. In fact, for the sake of time we had to choose some electronic components characterised by high absorption. These components could be replaced by equivalent self-made circuits, expressly designed.

CsI(Tl) could be replaced by other scintillator materials, emitting photons with a similar wavelength ensuring the best PDE possible for the SiPM, and the crystals themselves could be modified in terms of shape and sizes. In particular, a new pyramidal crystal should be used to optimise Compton suppression.

Moreover, the SiPM provided by SensL for this project had a Photo Detection Efficiency (PDE) around 13% which is very low compared to other photo-detector such as PMT. SensL is now commercialising a SiPM with a PDE of 35% at the same wavelength and this new device could be used in future work.

In Fig.9.1 here below the view of the final set-up of our device is presented.

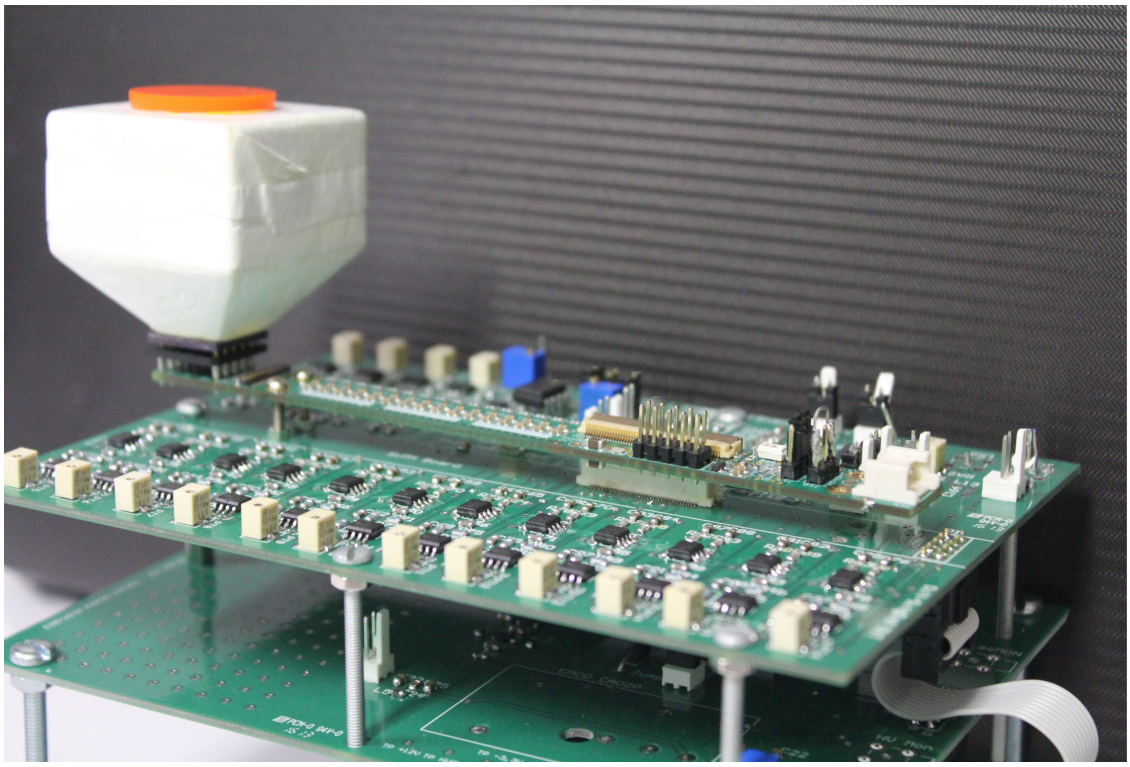

Fig. 9.1: View of the final set up of the device: the radioactive source is placed on the top of the scintillator crystal which in turn is positioned on the SiPM. You can clearly see the preamplifier board where the SiPM takes place and both the signal processing and power supply boards (top and bottom).

Appendix

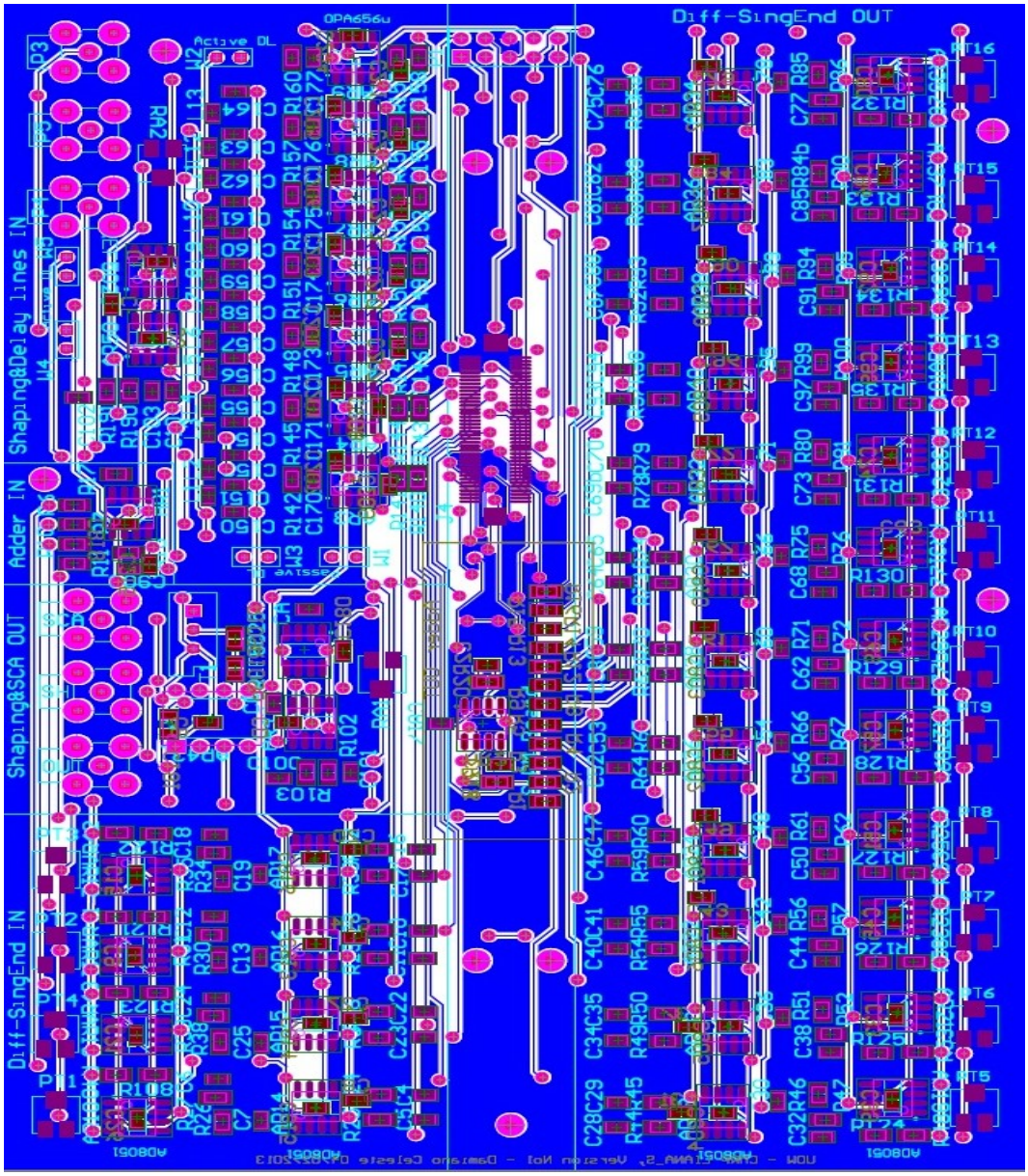

Fig. 2: Project file of the version No.1 of the signal processing board.

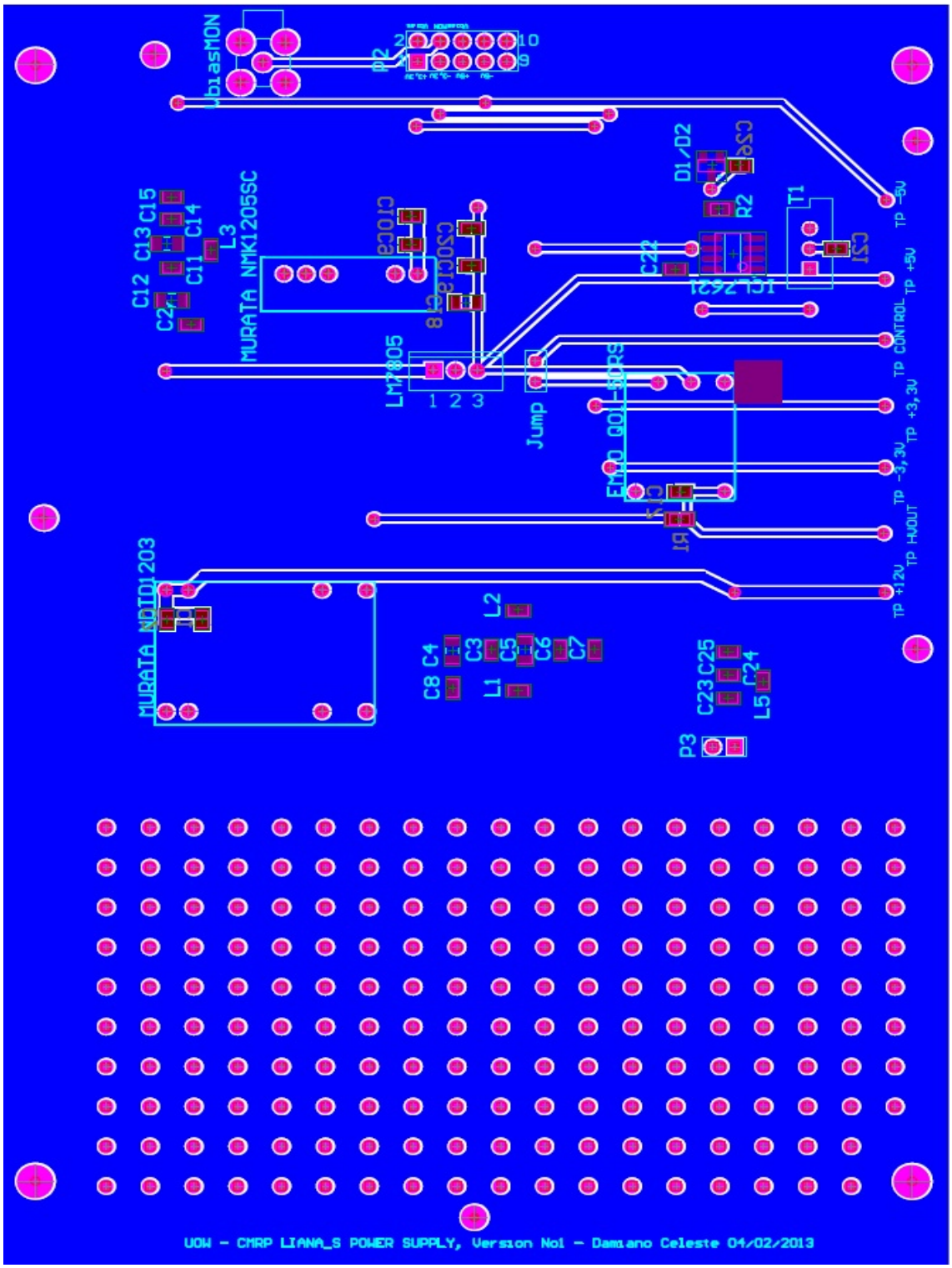

Fig. 3: Project file of the version No.1 of the power supply board.

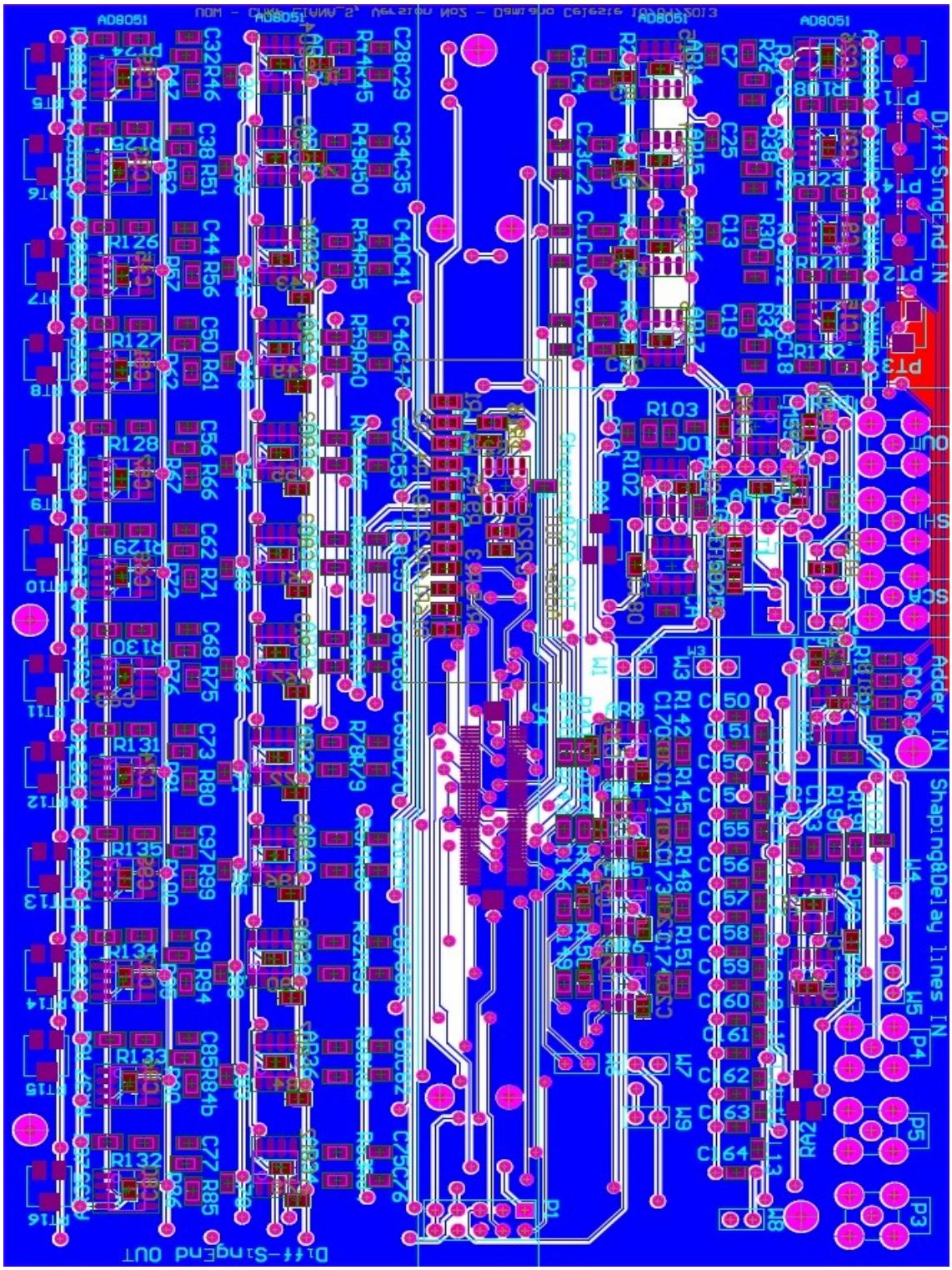

Fig. 4: Project file of the version No.2 of the signal processing board.

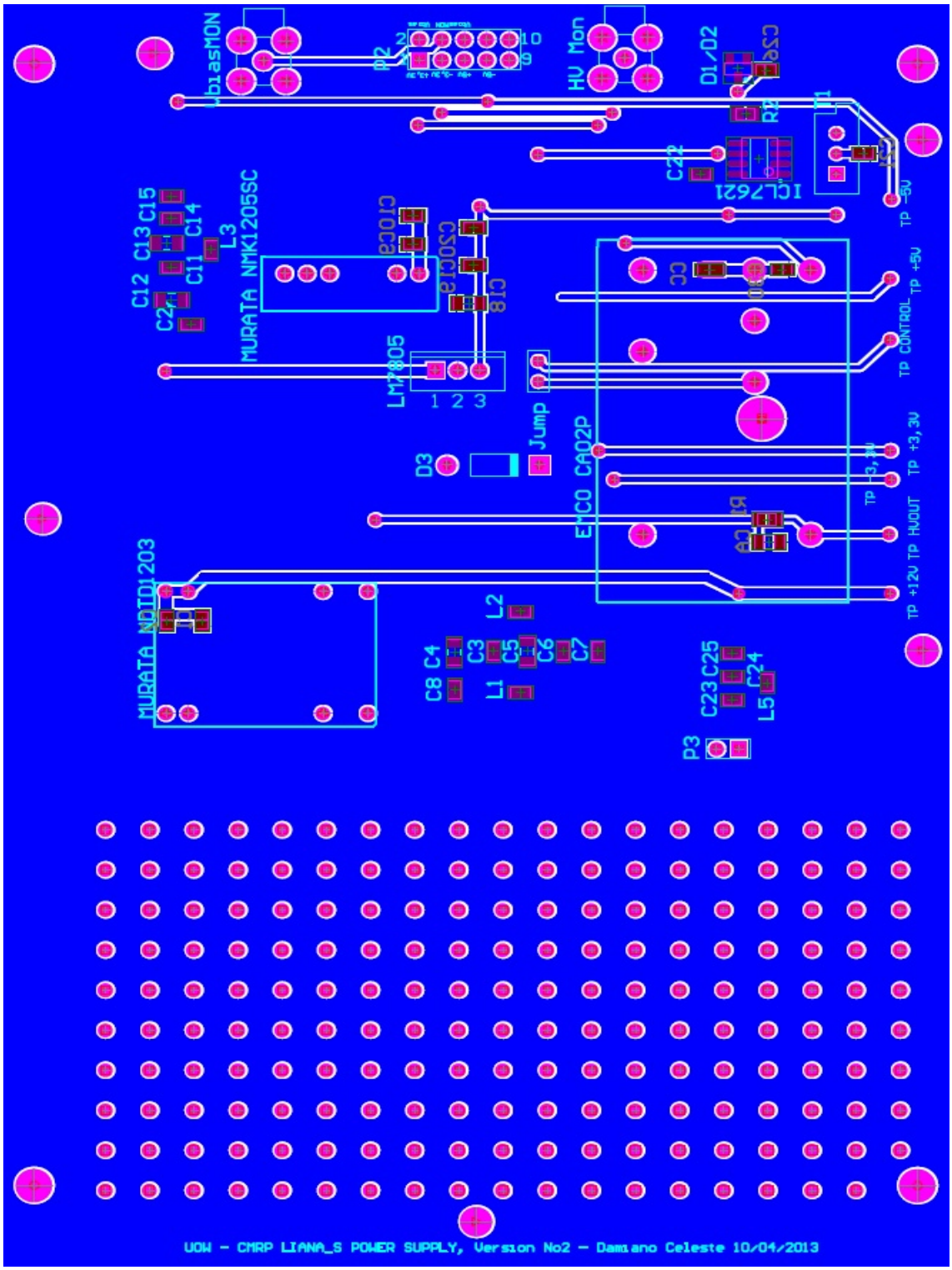

Fig. 5: Project file of the version No.2 of the power supply board.

Bibliography

[1] Weihua Zhang, Jing Yi, Pawel Mekarski,Kurt Ungar, Barry Hauck, Gary H. Kramer, *Quantification of U235 and U238 activity concentrations for undeclared nuclear materials by a digital gamma-gamma coincidence spectroscopy*, Applied radiation and isotopes, 69(2011)

[2] Han Soo Kim, Jang Ho Ha, Se Hwan Park, Seung Yeon Cho, Yong Kyun Kim, *Fabrication and performance characteristics of a CsI(Tl)/PIN diode radiation sensor for industrial application*, Applied radiation and isotopes, 67(2009)

[3] http://www.polimaster.com/products/hand_held_radionuclide_identification_devices_rids_/pm1401k_identifier/, *PM1401K Handheld radionuclide identification device principal features*, Polimaster

[4] http://www.smithsdetection.com/RadSeeker.php, *Radseeker-Handheld radiation detector and identifier principal features*, Smiths Detection

[5] http://www.atomtex.com/en/products/radionuclide-identification-devices-rids/at6102-and-at6102a-spectrometers, *AT6102, AT6102A Spectrometers principal features*, ATOMTEX.

[6] http://www.polimaster.com/products/hand_held_radionuclide_identification_devices_rids_/pm1410_identifier/, *Radioisotope identifier PM1410 principal features*, Polimaster, 2012

[7] Peter F. Bloser, Jason S. Legere, Luke F. Jablonski, Christopher M. Bancroft, Mark L. McConnell, James M. Ryan, *Silicon Photo-Multiplier readouts for scintillator-based Gamma-ray detectors in space*, IEEE 2010.

[8] Kuen Lee, J.W. Martin, A.B. Garson, M. Beilicke, Q. Guo, Q. Li, G. De Geronimo, M. Groza, A. Burger, H. Krawczynski, *Development of X-ray and Gamma-ray CZT detectors for Homeland Security applications, Detection and sensing of mines, explosive objects and obscured targets*, Vol 7664/766423, 2010.

[9] D.S. Judson, A.J. Boston, P.J. Coleman-Smith, *Compton imaging with the PorGamRays spectrometer*, Nuclear instruments and methods in physics research, 652(2011)

[10] Carolyn E. Seifert, Mitchell J. Myjak, David V. Jordan,*Simulated performance of the GammaTracker CdZnTe handheld radioisotope identifier*, 2007 IEEE Nuclear Science Symposium Conference Record.

[11] R. Aryaeinejad, D.F. Spencer, *Stand-alone and network capable pocket radiation detection system*, Nuclear Instruments and methods in physics research, 600(2009).

[12] The American National Standard Institute, *The National Committee on Radiation Instrumentation*, American national standard performance criteria for handheld instruments for the detection and identification of radionuclides, IEEE, 22 Jan 2007.

[13] G.F. Knoll, *Radiation detection and measurement*, Third edition 2000, John Wiley & Sons, Inc.

[14] K.S. Krane, *Introductory nuclear physics*, Rev. second edition 1988, john Wiley & Sons, Inc.

[15] F. Corsi, C. Marzocca, A. Perrotta, et al., *Electrical characterisation of Silicon Photomultiplier detectors for optimal front-end design*, IEEE Nuclear Science Symposium Conference Record, 2006.

[16] C. Piemonte, R. Battiston, M. Boscardin, et al., *Characterisation of the first prototype of Silicon Photomultiplier fabricated at ITC-irst*, IEEE Transaction on Nuclear Science, Feb. 2007.

[17] C. Piemonte, M. Boscardin, G.F. Dalla Betta, et al., *Recent developments on Silicon Photomultipliers produced at FBK-irst*, IEEE Nuclear Science Symposium Conference Record, 2007.

[18] N. Dinu, R. Battiston, M. Boscardin, et al., *Development of the first prototypes of Silicon Photomultiplier (SiPM) at ITC-irst*, Nuclear Instruments and Method in Physics Research, Nov. 2006.

[19] J. Eberth, J. Simpson, *From Ge(Li) detectors to gamma-ray tracking arrays-50 years of gamma spectroscopy with germanium detectors*, Progress in particle and nuclear physics, 2008. 60(2):p. 283-337

[20] T.H. Riedel, R. Feilitzsch, *Anticompton spectrometer element studies*, Applied Radiation and Isotopes, 2000, 53: p.5.

[21] J.A. Kulisek, et al., *Design and preliminary Monte Carlo calculations of an active Compton-suppressed LaBr3(Ce) detector system for TRU assay in remote-handles wastes*, Nuclear Instruments and methods in Physics Research Section A: Accelerators, spectrometers, detectors and associated equipment, 2007. 580(1): p.226-229.

[22] R. Aryaeinejad, J.K. Hartwell, W.W. Scates, *High-resolution Compton-suppressed CZT and LaCl3 detectors for fission products identification*, U.S. government work not protected by U.S. copyright.

[23] Yuan-qing Fan, et al., *The coincidence-summing correction of the Compton-suppression spectrometer*, Applied radiation adn isotopes, 70-2012: p.2124-2126.

[24] D.J. Herbert, et al., *Study of SiPM as a potential photo-detector for scintillator readout*, Nuclear instruments and methods in physics research A, 567-2006: p.356-359.

[25] Guen Bae Ko, et al., *Development of a front-end analog circuit for multi-channel SiPM readout and performance verification for various PET detector designs*, Nuclear instruments and methods in physics research A, 703-2013: p. 38-44.

[26] D. Pauwels, at al., *(221) Silicon photomultipliers in PET and hadron therapy applications*, ICTR-PHE, 2012, S111.

[27] G. Llosà, J. Barrio, C. Lacasta, et al., *First tests in the application of silicon photomultiplier arrays to dose monitoring in hadron therapy*, Nuclear instruments and methods in physics research A, 648-2011: p.S96-S99.

[28] T. Nakamori, T. Enomoto, T. Toizumi, et al., *Development of X-ray/gamma-ray imaging spectrometers using reach-through APD arrays*, IOP Publishing for Sissa Medialab, 20th of March 2012.

[29] M. Grodzicka, et al., *2x2 MPPC arrays in gamma spectrometry with CsI(Tl), LSO:Ce(Ca), LaBr3, BGO*, IEEE Nuclear science symposium conference record, 2011.

[30] M. Petasecca, B. Alpat, G. Ambrosi, et al., *Thermal and electrical characterisation of Silicon Photomultipliers*, IEEE Transaction on nuclear science, Vol.55, No3, June 2008.

[31] A. Flynn, *Investigation and characterisation of a dual anti-Compton probe for anti-terrorism applications*, CMRP-University of Wollongong, 2011.

[32] Canberra, *Compton suppression...made easy*, 1998 [Available from: http://www.canberra.com/literature/gamma_spectroscopy/application_notes /comptonsupp.pdf]

[33] G. Biondo, E. Sacchi, *Manuale di elettronica e telecomunicazioni*, Quarta edizione Hoepli, 1996.